

The Galactic Chemical Evolution of Carbon
Implications for Stellar Nucleosynthesis

Undergraduate Research Thesis

Presented in partial fulfillment of the requirements for graduation *with research distinction in Astronomy and Astrophysics* in the College of Arts and Sciences of
The Ohio State University

by

Daniel Alexander Boyea

The Ohio State University
April 2023

Project Advisors
James W. Johnson, Department of Astronomy
Professor David H. Weinberg, Department of Astronomy

Abstract

Limited knowledge of stellar physics leads to uncertainties in elemental yield predictions. As an independent approach, I constrain the nucleosynthetic yields of C using multizone Galactic chemical evolution models. By matching the median trends of $[C/Mg]$ - $[Mg/H]$ and $[C/Mg]$ - $[Mg/Fe]$ in APOGEE subgiant stars, I find that high-mass and low-mass stars contribute $\sim 80\%$ and $\sim 20\%$ of total C production respectively. To match the normalization of the trends, I estimate the massive star C/Mg yield ratio $y_C^{CC}/y_{Mg}^{CC} = 1.57 + 0.59 (Z/Z_\odot)$, explaining the $[C/Mg]$ - $[Mg/H]$ trend when including the low mass C contribution. Variations in the star formation history only slightly impact the low $[Mg/Fe]$ tail of the $[C/Mg]$ - $[Mg/Fe]$ relation. However, most of the scatter in the $[C/Mg]$ - $[Mg/H]$ distribution can be attributed to measurement errors and radial migration. Due to the degeneracy between the normalization of elemental yields and the strength of mass-loading in Galactic outflows, I am only able to constrain the relative yields of C/Mg and its metallicity dependence. While measurements of gas-phase C abundances are challenging, my model is broadly consistent with the $[C/O]$ - $[O/H]$ trend observed in compiled literature measurements.

Acknowledgements

I hope that the people who helped me complete this project will appreciate how much they have helped me. This year has been an incredibly challenging journey—and perhaps I am not open enough about what it has been like. I undoubtedly would not have reached this day without everyone's help.

James Johnson—your mentorship and guidance throughout this project was critical. You helped me learn an incredible amount about being an astronomer, and I am forever grateful for how you have guided this project, through late nights and last-minute comments. Wayne, for everything you do for everyone—you are the glue holding together our department and nobody can say thank you enough. David and Jennifer for helping this project move forward, by providing guidance at critical junctions and being part of my committee. RVA, for being the non-astronomer forced to listen to my thesis and providing valuable feedback about the understandability of this work.

Even though you may have not been able to help me with the science, dear friends and family, you have been no less important in the completion of this work. Eric, even across the country, you have always been a point of support and stability, and I am always happy to be around you. Anya, you are a wonderful friend and I cannot thank you enough for your unconditional support this year. All my friends who are just wonderful, inspiring, and incredible people—Kaia, Maria, Mary, Autumn, Simon, Bailee, Aaliyah, Sanskruti, Alyssa, Harrison, Denis, Natalia, Keith, and so many others. And my family (including Arya, my most lovable doodle)—I can not even begin to thank you enough for simply helping me recover my health and make it to graduation.

Table of Contents

Abstract	i
Acknowledgements	ii
List of Figures	v
List of Tables	vi
1 Introduction	1
2 Nucleosynthesis	4
2.1 Asymptotic Giant Branch Stars	5
2.2 Core Collapse Supernovae	8
3 The Equilibrium Approximation	11
3.1 Yield Models	12
3.2 Uncertainties	13
4 The Multizone Model	16
5 Multizone Model Results	18
5.1 Data Selection	18
5.2 The Evolution of Carbon Abundances in the Galaxy	18
5.3 Low and High-Mass Stellar Yields	19
5.4 Star Formation History	22
5.5 Outflows	24
5.6 Scatter	25
5.7 Gas-Phase Abundances	27
6 Conclusions	30

Bibliography	32
A The Subgiant Sample	40
B Low-Mass Stellar Evolution	43
C Oxygen and Magnesium	45
D Software	46
E Low-Mass Stellar Yield Models	47
F Symbols	48
Acronyms	50
Glossary	51

List of Figures

1	Subgiant Abundances	3
2	Low-Mass Stellar Carbon Yields	7
3	Carbon Delay Time Distribution	7
4	Low-Mass-Star Yield Metallicity Dependence	8
5	High-Mass Star Carbon Yields	10
6	Reverse-Fit Yields	14
7	Carbon Chemical Evolution Tracks	20
8	Median Stellar Abundance Trends	21
9	Adjusted Yield Models	23
10	Alternate Star-Formation-History Models	24
11	Reduced-Outflow Models	25
12	Scatter Agreement	26
13	C/N Abundance Agreement	28
14	Gas-Phase Abundances	29
15	Subgiant Selection	42
16	O/Mg Yields	45

List of Tables

1	Fiducial Model Yields	5
2	Low-Mass Stellar Carbon Yields at Solar Metallicity	22

1. Introduction

Galactic chemical evolution (GCE) aims to understand the chemical enrichment and star formation histories of galaxies. At the core of GCE models are stellar yields—the amount of each chemical element stars synthesize. Each element is produced in different amounts by different stars, leaving traces of the Galaxy’s evolutionary history. Through *Galactic Archeology*, we can reconstruct the history of our galaxy by investigating clues left behind in stars.

Here, I aim to understand C enrichment—where it is produced and how its abundances evolve. C is unique nucleosynthetically, one of few light elements (along with N) produced in asymptotic giant branch (AGB) stars (e.g. Johnson 2019; Karakas & Lattanzio 2014). C and N are well-studied elements since they are easy to observe in stellar spectra, even at the lowest metallicities (e.g. Fabbian et al. 2009; Nissen et al. 2014; Lambert & Ries 1981; Laird 1985; Lambert et al. 1986). Additionally, C and N are used as age indicators in red giant branch stars (Martig et al. 2016; Masseron & Gilmore 2015; Hasselquist et al. 2019; Vincenzo et al. 2021).

Gas-phase [C/O] ratios¹—observed in very low metallicity,² high redshift³ damped Lyman-alpha systems (DLA)—decrease with increasing [O/H] (Frebel & Norris 2015; Cooke et al. 2017). Then, [C/O] increases above [O/H] ≈ -1 (Berg et al. 2019; see discussion in section 5.7). While we know C is produced in AGB stars and core collapse supernovae (CCSNE), we still have a limited understanding of the magnitude and metallicity-dependence of each process.

Nucleosynthetic yields predicted by stellar evolution models are rife with uncertainties, despite their central role in GCE models. The production rates of elements in stars are shaped by poorly understood processes, including mass loss,

¹In this paper, I use the standard notation for chemical abundances. $[A/B] = \log_{10}(A/B) - \log_{10}(A_{\odot}/B_{\odot})$, i.e. $[A/B]$ is the logarithm of the ratio between A and B, scaled such that $[A/B] = 0$ for the sun. Solar abundances are as measured in Asplund et al. (2009).

²Astronomers are not chemists. By metallicity, I mean the (mass) fraction of any element which is not H or He, denoted by Z . For the sun, $Z_{\odot} = 0.014$.

³i.e. observed in the early universe.

nuclear reaction rates, rotational mixing, convection, and explodability (Karakas & Lattanzio 2014; Ventura et al. 2013; Limongi & Chieffi 2018; Griffith et al. 2021).

GCE models typically use unmodified nucleosynthetic predictions and attempt to match observations by varying the star formation history (SFH) and other evolutionary parameters. Here, I introduce C yields as an additional free parameter, determining which yield prescriptions reproduce Galactic abundance trends. Johnson et al. (2023) examined similar GCE models of N, an element whose production is closely related to C. They found that trends in N and O abundances can be explained by the metallicity dependence of relative N and O yields. Here, I extend their models to C, deriving similar constraints on C/Mg yields. I assess which yield prescriptions reproduce Galactic abundance trends while investigating the impact of GCE model assumptions, such as SFH and outflow mass loading.

C abundances are challenging to measure. When a star enters the red giant branch, material from the CNO-processed core is mixed with the envelope in first dredge up, enhancing N and depleting C (Iben 1967; Vincenzo et al. 2021; Karakas & Lattanzio 2014). Measurements of these evolved stars' atmospheres will no longer reflect their birth abundances. Additionally, gas-phase measurements of C are extremely limited as C lacks strong lines in HII regions (Skillman et al. 2020).

As my observational constraint, I use a sample of subgiant stars from the Apache Point Observatory Galactic Evolution Experiment (APOGEE) (Majewski et al. 2017). According to stellar evolution theory and observations (Gilroy 1989; Korn et al. 2007; Lind et al. 2008; Souto et al. 2018, 2019), these stars have not yet experienced first dredge up but have well-mixed envelopes. So, their surface abundances should thus represent their birth composition. In Fig. 1, I plot this sample, selected by the criteria in Roberts et al. (2023, in prep; see Appendix A). In this sample, $[C/Mg]$ increases with metallicity, and $[C/Mg]$ decreases with $[Mg/Fe]$ at fixed $[Mg/H]$. Using these trends, I will develop a model of the enrichment sources and evolution of C.

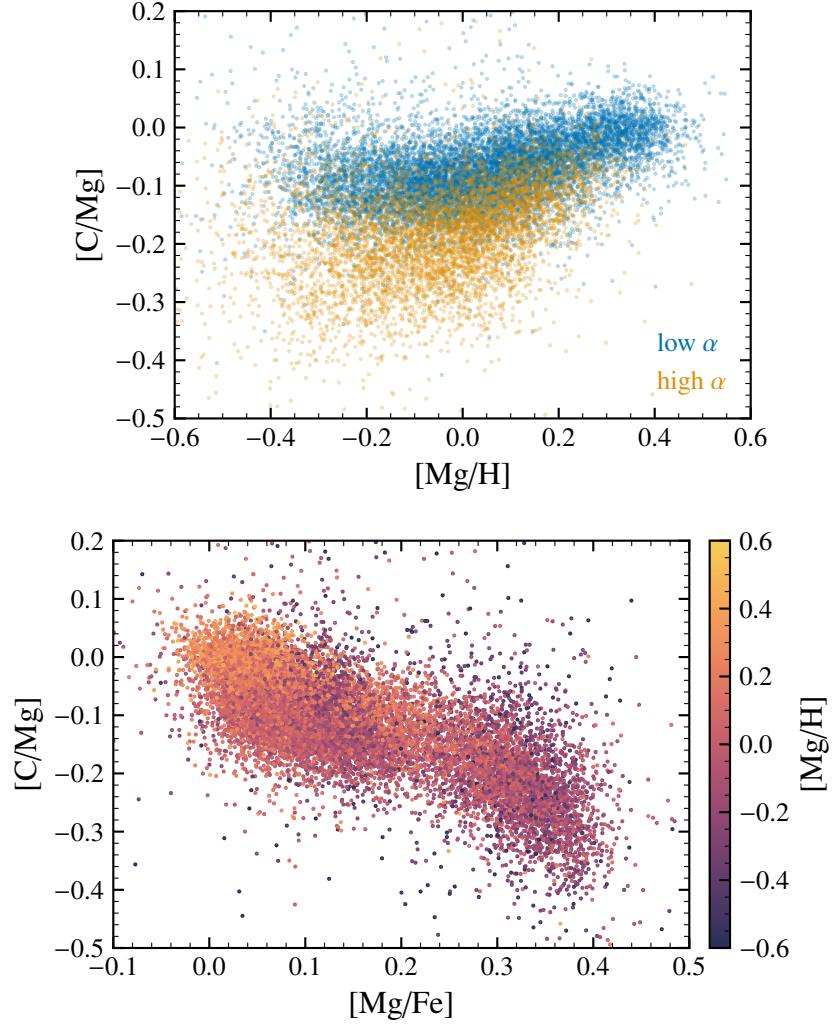


Figure 1: The $[C/Mg]$ ratio against $[Mg/H]$ (top) and $[Mg/Fe]$ (bottom) for the Roberts et al. (2023, in prep.) sample of APOGEE subgiants. On the top, I plot high and low- α stars in blue and orange, using the separation defined in Equation 21 (the high and low- α stars are named for their high or low α -element to Fe ratios, or in this case, Mg/Fe). On the bottom, I color-code stars according to their $[Mg/H]$ abundance.

2. Nucleosynthesis

Theoretical models of stellar nucleosynthesis provide the starting point of this investigation. I focus on three primary nucleosynthetic pathways: AGB stars, CCSNE, and type Ia supernovae (SNE Ia). Each process has unique timescales and yields, traceable through the tools of GCE. C is produced in both CCSNE and AGB stars. I also compare C to Mg and Fe, which trace CCSNE and SNE Ia respectively.

When a single stellar population (SSP) forms, CCSNE are the first enrichment event. CCSNE explode within $\lesssim 40$ Myr, providing light elements (C, O, and Mg) and heavier elements (Fe and beyond). O and Mg are produced almost entirely from CCSNE with metallicity-independent yields. Next, low-mass stars begin to reach the end of their lives. By shedding their outer layers, AGB stars are important sources of C, N, and neutron capture elements. Finally, white dwarfs explode, releasing Fe and other iron-peak elements.

For an element X and star with mass M , the net-fractional stellar yield \tilde{y} is defined as the net production of new X relative to M , or

$$\tilde{y}_X = \frac{M_{X, \text{ejected}} - Z_{0,X} M_{\text{ejected}}}{M} \quad (1)$$

where M_{ejected} and $M_{X, \text{ejected}}$ are the total ejected mass of the envelope and the element X , respectively. For example, if a $1 M_{\odot}$ star has $\tilde{y}_C = 10^{-3}$, then the star will add $10^{-3} M_{\odot}$ of new C to the interstellar medium. Although per-star yields are necessary to compute AGB star enrichment rates in GCE models, IMF-averaged yields are useful in interpreting their predictions. For a yield y from a star of mass M and initial metallicity Z , the IMF-averaged yield is given by

$$y_X(Z, t) = \int_{M_{\min}(t)}^{M_{\max}} \tilde{y}_X(M, Z) \frac{dN}{dM} dM \quad (2)$$

where dN/dM is the normalized initial mass function (IMF), $M_{\max} = 100 M_{\odot}$ is the maximum stellar mass, and $M_{\min}(t)$ is the mass of stars with lifetime t .¹ I use

¹In my model, the mass-lifetime relation is $\log \tau_M = 1.02 - 3.57 \log M + 0.90 (\log M)^2$, where τ_M is in Gyr, from Larson 1974. For AGB stars, the stellar yields are truncated above $8 M_{\odot}$.

Table 1: Yields for the fiducial model (in units of ssp birth mass). See Section 2.1 for the definition of C11.

Element	y_{C}^{CC}	\tilde{y}^{AGB}	y^{SNeIa}
C	$0.0028 + 0.001 (Z/Z_{\odot})$	$2.9 \times \text{C11}$	0
Mg	0.00185	0	0
Fe	0.0012	0	0.00214
N	0.00072	$9 \times 10^{-4} (Z/Z_{\odot}) M$	0

$t = 10$ Gyr for total yields when t is not used. To calculate the IMF-averaged net yields, I use the Versatile Integrator for Chemical Evolution code (VICE²).

To focus on C yields, I adapt the yield choices of other elements from Johnson et al. (2021, 2023). Table 1 contains my fiducial yields, in units of a ssp’s birth mass. Also following Johnson et al. (2021, 2023), I take the SNE Ia delay time distribution to be a $t^{-1.1}$ power-law suggested by the observations of Maoz et al. (2012).

2.1 Asymptotic Giant Branch Stars

An AGB star is a low-mass star ($\lesssim 8M_{\odot}$) during its final phase of evolution (see Appendix B). In an AGB star, two competing processes determine the outcome of C production: third dredge up and hot bottom burning. Third dredge up accompanies thermal pulses in AGB stars, where material from the CO core is mixed with the envelope, increasing surface C abundances (Karakas & Lattanzio 2014). If this envelope is lost during the AGB phase, then C yields are enhanced. Hot bottom burning is the activation of proton capture reactions and the CNO cycle at the base of the convective envelope. Because the ^{14}N proton capture is the slowest component of the CNO cycle (Adelberger et al. 2011), the CNO cycle converts nearly all ^{12}C into ^{14}N . As a result, when both third dredge up and hot bottom burning occur, ^{12}C yields are lowered (see discussion in Johnson et al. 2023 and Ventura et al. 2013).

In this work, I explore four different sets of AGB star yield tables from literature, providing well-sampled grids in metallicity and mass for use in chemical evolution models.

- C11: Cristallo et al. (2011, 2015)

²VICE is available at <https://github.com/giganano/VICE>

- K10: Karakas (2010)
- V13: Ventura et al. (2013, 2014, 2018, 2020)
- K16: Karakas & Lugaro (2016); Karakas et al. (2018)

For my models to match observations, I find that need to uniformly amplify these yield tables (see Eq. 12). I use C11 table, amplified by a factor of 2.9, as the fiducial AGB yield.

Fig. 2 compares the stellar AGB C yield $\tilde{y}_C^{\text{AGB}}(M, Z)$ for these four models. The yields may be negative if a star ejects material with a lower average C abundance than the material the star was formed from. Most models agree on the qualitative shape of the net fractional AGB C yield—stars with masses between $\sim 2 M_\odot$ and $\sim 4 M_\odot$ have the highest fractional C yields, with the mass of the peak increasing and overall yields decreasing with increasing Z . High mass, high Z stars destroy ^{12}C because they experience both third dredge up and hot bottom burning, but the latter is much more efficient.

Fig. 3 shows the total production of C by AGB stars in a SSP at an age t , i.e. $\tilde{y}_C(Z_\odot, t)$. As the mass range $2 M_\odot \lesssim M \lesssim 4 M_\odot$ is most important for C production, about half of C production occurs before ~ 1 Gyr, similar to SNE Ia Fe. K10 and K16 weight C production more heavily towards high-mass stars resulting in a faster enrichment delay time, whereas the C11 and V13 models predict a slightly longer timescale of ~ 1 Gyr. In any case, little to no C is produced more than 2 Gyr after a star formation event. This is in contrast to Fe whose production lasts up to 10 Gyr after a star formation event. As shown in the right panel of Fig. 3, with increasing Z , C enrichment occurs earlier, and C destruction in low-mass stars leads to a declining C abundance at late times.

Fig. 4 shows IMF-averaged C yields for each AGB model as a function of metallicity Z . V13 differs in that it shows a non-monotonic metallicity dependence. However, this effect is only for models with $\log Z/Z_\odot \lesssim -1$. Otherwise, models differ only in their yield normalization and metallicity dependence. All models predict yields within a factor of ~ 2 for fixed metallicity. For example, the three models C11, K10, and K16 predict y_C^{AGB} to be between 0.006 and 0.008 at solar metallicity, but C11 has a much shallower metallicity dependence than the K10 and K16 models. V13 instead predicts a yield ~ 0.004 .

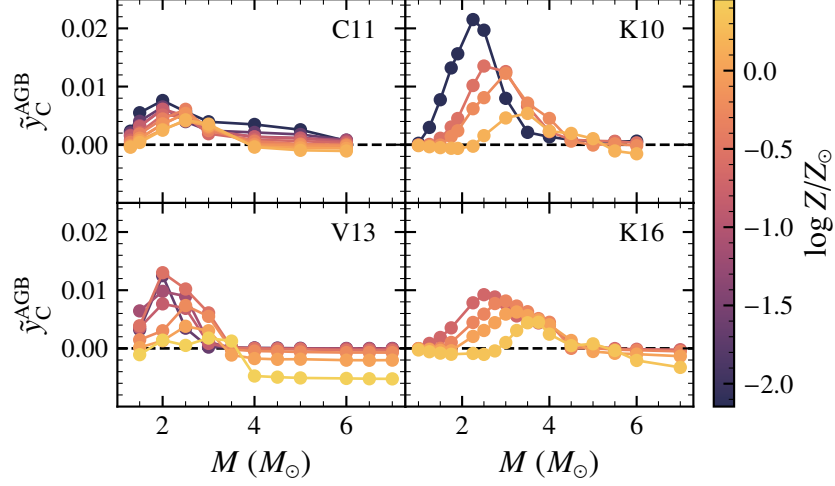


Figure 2: The net fractional AGB C yield plotted as a function of initial stellar mass M and color-coded according to metallicity. The black dashed line shows $\tilde{y} = 0$ for reference. Each panel represents yields from one of four AGB models: C11, K10, V13, K16 (see Section 2.1 and Appendix E).

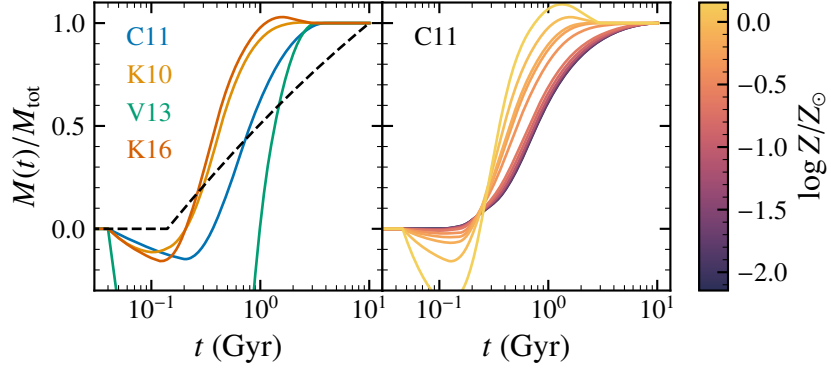


Figure 3: C production by AGB stars as a function of SSP age, normalized to the total mass M_{tot} produced at $t = 10$ Gyr. **Left:** The four AGB yield models from literature at solar metallicity (C11, K10, V13, or K16). The delay time distribution of type Ia supernovae ($\propto t^{-1.1}$) is plotted as a dashed black line for comparison. **Right:** The C11 AGB model at different metallicities.

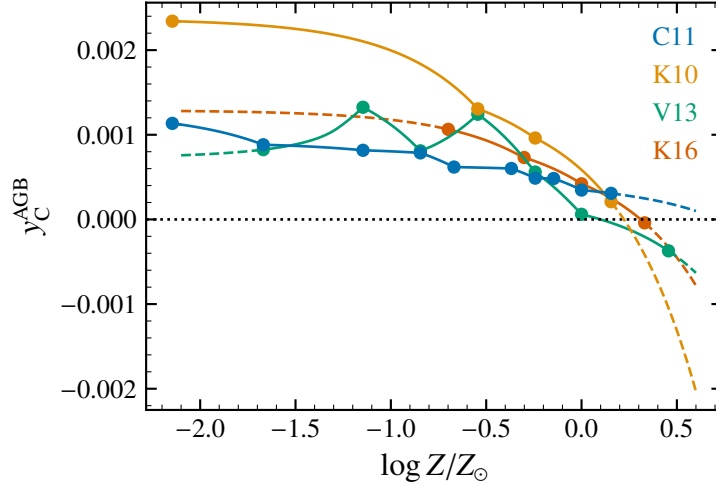


Figure 4: The net fractional IMF-weighted AGB C yield y_C^{AGB} as a function of metallicity for each of our AGB yield models. (y_C^{AGB} is the net mass of C produced by AGB stars per unit mass of star formation, after 10 Gyr and assuming a Kroupa 2001 IMF.)

2.2 Core Collapse Supernovae

Massive stars form ^{12}C in their cores through the triple- α process (see Appendix B). However, only C ejected through supernovae and stellar winds contributes to the yield. While there are many stellar models providing predictions of CCSNE yields, the results of these models are highly uncertain due to the many stellar modeling uncertainties.

Fig. 5 plots calculations of the IMF-integrated yields, defined with Eq. 2 (computed using VICE’s `vice.yields.ccsne.fractional` function). CCSNE models predict a wide range of C yields, spanning almost a factor of ten. Both the Nomoto et al. (2013) and Limongi & Chieffi (2018) models show positive metallicity dependence. The Limongi & Chieffi (2018) models also include rotation, showing that variations in the rotational velocity of the star can dramatically increase the magnitude and metallicity dependence of y_C^{CC} . Rotation induces more mixing allowing the CO core to grow larger. As I will later show, CCSNE C production needs to be strongly metallicity-dependent at $Z/Z_\odot \approx 1$, which is consistent with the Limongi & Chieffi (2018) rapidly rotating models.

Fig. 5 shows the C11 AGB model for comparison on the top. Especially at

$Z \approx Z_{\odot}$, most *ccsne* models dominate AGB C production. Later, I will also show empirically this is the case. On the bottom of Fig. 5, I also show the *ccsne* [C/Mg] ratio, defined by

$$[\text{C/Mg}]^{\text{cc}} = \log_{10} \left(\frac{y_{\text{C}}^{\text{cc}}}{y_{\text{Mg}}^{\text{cc}}} \right) - \log_{10} \left(\frac{Z_{\text{C}, \odot}}{Z_{\text{Mg}, \odot}} \right). \quad (3)$$

$[\text{C/Mg}]^{\text{cc}}$ describes what [C/Mg] would be if *ccsne* were the only process producing C. Once again, different *ccsne* models span a large range in [C/Mg]. I chose to instead parameterize y_{C}^{cc} to enable agreement with observations, as most *ccsne* models fail to achieve near-solar [C/Mg]. Assumptions about the explodability landscape affect C and Mg production. Increasing the fraction of stars that explode increases y_{C}^{cc} , as stars that directly collapse do not contribute to explosive yields (Griffith et al. 2021). However, C is relatively unaffected by the black-hole landscape, as very massive stars contribute C through enriched winds. Since Mg is formed deeper in the core of high-mass stars, the Mg yield drops much more steeply, so models where few stars explode (S16/W18) have higher [C/Mg].

Ccsne models also do not reach [O/Mg] due to overproduction of O or underproduction of Mg, or both (Griffith et al. 2021). Here, I assume [O/Mg] = 0, which is not compatible with *ccsne* models but is consistent with *APOGEE* observations (Weinberg et al. 2019, 2022).

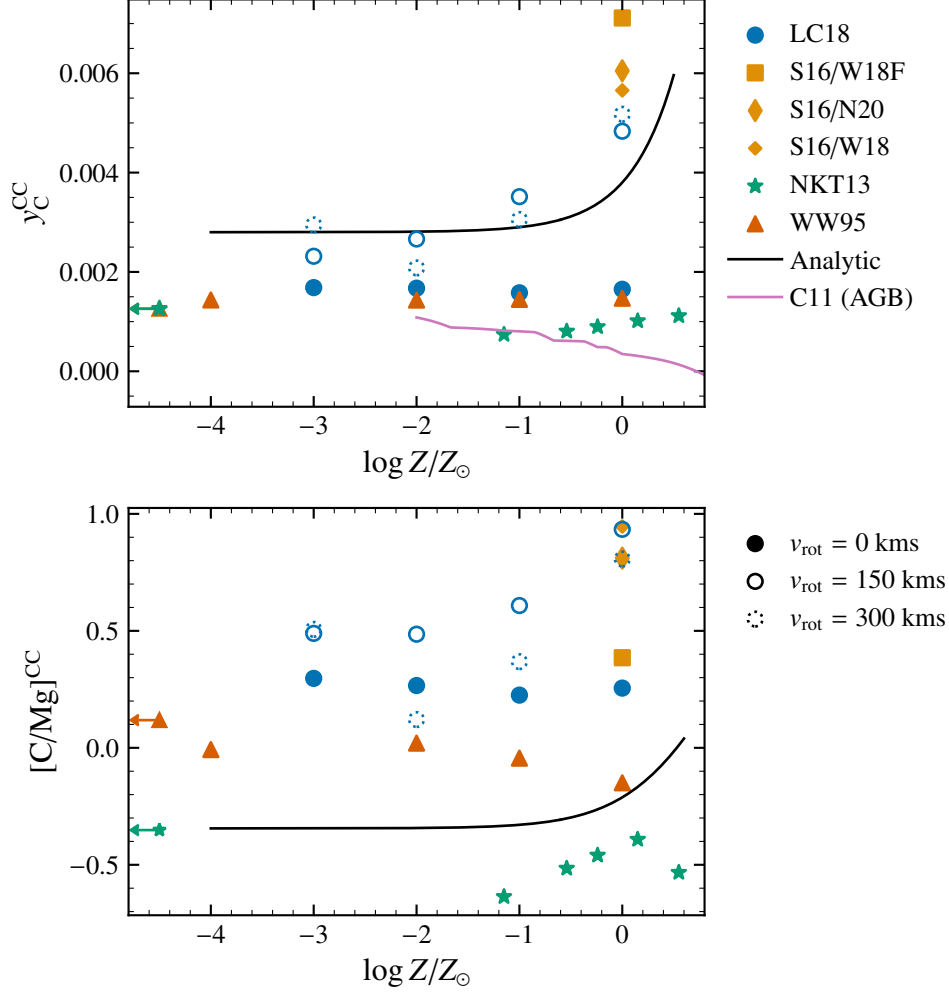


Figure 5: C yields from high-mass stars. **Top:** The IMF-weighted CCSNE yield of C as a function of metallicity. **Bottom:** The CCSNE $[C/Mg]$ abundance ratio, defined in Eq. 3. The black line is the derived C yield from Section 3, $y_C^{\text{CC}} = 0.0028 + 0.001(Z/Z_{\odot})$. Yields are shown for tables from Woosley & Weaver (1995; red triangles), Sukhbold et al. (2016; orange squares and diamonds), Nomoto et al. (2013; green stars), and Limongi & Chieffi (2018; blue circles). Sukhbold et al. (2016) report yields for different black hole landscapes, while Limongi & Chieffi (2018) provide yields at different rotational velocities. In the top panel, the pink line denotes y_C^{AGB} from C11 for comparison. All models include wind yields.

3. The Equilibrium Approximation

In the presence of metal-poor gas accretion and feedback-driven outflows, galaxies reach an equilibrium abundance in which production of new metals is balanced by losses to new stars and outflows (Larson 1972; Dalcanton 2007; Finlator & Davé 2008; Peeples & Shankar 2011; Lilly et al. 2013). While our galaxy is likely not in perfect equilibrium or described by a single, homogeneous chemical region, the equilibrium approximation is nevertheless useful in understanding yields and metallicity dependence (e.g. Johnson et al. 2022, 2023; Weinberg et al. 2017).

I assume a simple *one-zone* chemical evolution model (e.g. Tinsley 1980; Pagel 2009; Matteucci 2021). Newly produced metals are homogeneously and instantaneously mixed, so spatial dependence is neglected. I define M_X to be the mass of element X in the gas-phase, \dot{M}_\star to be the star formation rate (in $M_\odot \text{ yr}^{-1}$), and η to be the mass loading factor $\eta \equiv \dot{M}_{\text{outflow}}/\dot{M}_\star$ (representing the strength of outflows). A SSP returns a fraction r of their birth mass to the interstellar medium, due to ejected stellar envelopes.¹ Given the IMF-averaged yield of Mg y_{Mg} , the rate of change in the gas-phase mass of Mg is a simple sum of sources and sinks,

$$\dot{M}_{\text{Mg}} = y_X \dot{M}_\star - \dot{M}_{\text{Mg, remnants}} - \dot{M}_{\text{Mg, outflows}}, \quad (4)$$

where the first term on the right-hand side describes CCSNE enrichment. In terms of the return mass fraction of stars r , the mass lost to remnants is $Z_X \dot{M}_\star (1 - r)$. And, the outflows deplete mass at a rate $Z_X \dot{M}_\star \eta$. (I assume the composition of outflows is the same as the interstellar medium.) Substituting for η and r ,

$$\dot{M}_{\text{Mg}} = y_X \dot{M}_\star - (1 + \eta - r) Z_X \dot{M}_\star. \quad (5)$$

Assuming an exponentially declining star formation history $\dot{M}_\star \propto e^{-t/\tau_{\text{sfh}}}$, the equilibrium abundance is derived analytically by setting $\dot{Z}_{\text{Mg}} = 0$.

$$Z_{\text{Mg}}^{\text{eq}}(R) = \frac{y_{\text{Mg}}}{1 + \eta(R) - r - \tau_\star/\tau_{\text{sfh}}}, \quad (6)$$

¹ $r \approx 0.4$ for a Kroupa 2001 IMF.

where τ_\star is the star formation rate. (η depends on R to create a metallicity gradient. See also Section 4 and Eq. 16.) In the special case of constant star formation, $\tau_{\text{sfr}} \rightarrow \infty$, the denominator simplifies to $1 + \eta - r$.

Likewise, for AGB stars,² Eq. 6 then becomes

$$Z_{\text{C}}^{\text{eq}}(R) = \frac{y_{\text{C}}^{\text{CC}} + y_{\text{C}}^{\text{AGB}}}{1 + \eta(R) - r - \tau_\star/\tau_{\text{sfr}}} \quad (7)$$

And the equilibrium C/Mg abundance ratio is

$$\frac{Z_{\text{C}}^{\text{eq}}}{Z_{\text{Mg}}^{\text{eq}}} = \frac{y_{\text{C}}^{\text{CC}} + y_{\text{C}}^{\text{AGB}}}{y_{\text{Mg}}^{\text{CC}}}. \quad (8)$$

Analogous to Johnson et al. (2023) arguments about N, the trends in abundance ratios are set by yield ratios in these GCE models. The effect of other GCE parameters (most importantly η) cancels. As a consequence, yield ratios should establish abundance ratio trends in models which assume a different normalization of element yields and mass-loading (see discussion below). This argument can also be inverted to infer yields from abundance ratio trends. To the extent that observed C and Mg trends reflect the equilibrium abundances in different Galactic regions, we can infer the CCSNE yield given an assumed AGB star yield (or vice versa). Inferring y_{C}^{CC} from $y_{\text{C}}^{\text{AGB}}$,

$$y_{\text{C}}^{\text{CC}} = y_{\text{Mg}}^{\text{CC}} \frac{Z_{\text{C}, \text{eq}}}{Z_{\text{Mg}, \text{eq}}} - \langle y_{\text{C}}^{\text{agb}} \rangle \quad (9)$$

Rewriting this expression as a relative yield of C and Mg,

$$\frac{y_{\text{C}}^{\text{CC}}}{y_{\text{Mg}}^{\text{CC}}} = \frac{Z_{\text{C}, \odot}}{Z_{\text{Mg}, \odot}} 10^{[\text{C/Mg}]} - \frac{y_{\text{C}}^{\text{AGB}}}{y_{\text{Mg}}^{\text{CC}}}. \quad (10)$$

3.1 Yield Models

As I will discuss in Section 5.5, the normalization of yields and η is degenerate. This can be observed in Eq. 8, where changes in η or the scaling of $y_{\text{C}}/y_{\text{Mg}}$ would not affect equilibrium trends. Furthermore, in Eq. 6, an increase in both y_{Mg} and η would leave $Z_{\text{Mg}}^{\text{eq}}$ unchanged. My models here are unable to distinguish the overall

²In detail, the AGB contribution requires integration over the SFR to account for the finite lifetimes of stars. However, for this exponential SFR, this effect is minimal, so I simply use $y_{\text{C}}^{\text{AGB}}$ for the current AGB contribution.

scaling of yields and outflow mass loading. Choosing to keep y_C fixed reduces unnecessary free parameters. So, at solar metallicity, I set

$$y_C \big|_{Z=Z_\odot} = y_C^{\text{CC}} + y_C^{\text{AGB}} = 0.005 \quad (11a)$$

$$y_C/y_{\text{Mg}}^{\text{CC}} \big|_{Z=Z_\odot} = 2.7. \quad (11b)$$

This ratio results in an equilibrium abundance $[C/Mg] = -0.09$, which is consistent with the subgiant sample and is within $\sim 20\%$ of the solar C/Mg mixture from Asplund et al. (2009).

In Section 5.3, I will show that none of the four AGB yield sets (C11, K10, V13, K16) produce enough C relative to this y_C^{CC} value. So, I introduce normalization factors, α_{AGB} , and α_{CC} which denote a multiplicative scaling of y_C^{CC} and y_C^{AGB} respectively.

$$y_C^{\text{AGB}} \rightarrow \alpha_{\text{AGB}} y_C^{\text{AGB}} \quad (12a)$$

$$y_C^{\text{CC}} \rightarrow \alpha_{\text{CC}} y_C^{\text{CC}} \quad (12b)$$

$$\alpha_{\text{CC}} = \frac{y_C - \alpha_{\text{AGB}} y_C^{\text{AGB}}}{y_C^{\text{CC}}} \quad (12c)$$

Above, α_{CC} is dependent on the choice of α_{AGB} to keep the total C yield constant.

In Section 5.3, I find that $\alpha_{\text{AGB}} \approx 2.9$ for the C11 yield model. Using this AGB yield, I can now use Eq. 10 to find an estimate of y_C^{CC} as a function of metallicity. I show the values of y_C^{CC} I obtain from the subgiant sample in Fig. 6. From a regression analysis, I suggest here that

$$y_C^{\text{CC}} = 0.0028 + \zeta \left(\frac{Z}{Z_\odot} \right), \quad (13)$$

where $\zeta \approx 0.001$ describes the metallicity dependence.

3.2 Uncertainties

I only perform this analysis on the C11 yields because C11 has yields tables more finely sampled in metallicity than the other three AGB yield tables. As the metallicity range of the data is small ($-0.4 \lesssim [Mg/H] \lesssim 0.4$), other models are more challenging to interpret in this range. Furthermore, the APOGEE observations may have systematics. Other measurements of C abundances (e.g. Vincenzo et al. 2021) have slight disagreements in the overall shape of the trend (see Section

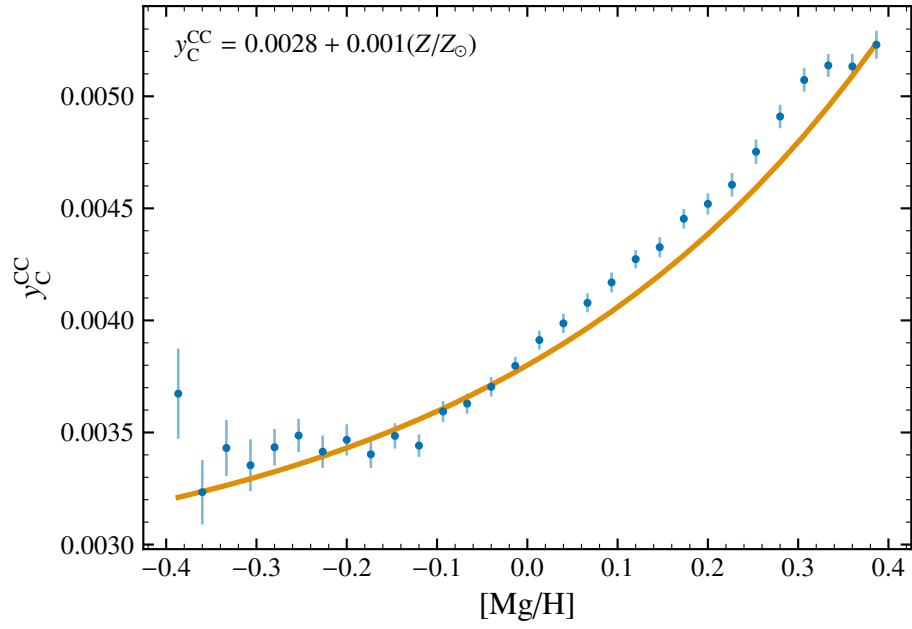


Figure 6: Inferred high-mass star C yields as a function of metallicity. I assume equilibrium and $3 \times \text{C11}$ AGB yields (orange curve, see discussion in Section 3). Blue points are the median value of y_C^{CC} for each bin in $[Mg/H]$ with uncertainties based on the median absolute deviation.

A). So, this expression of $y_C^{\text{CC}}/y_{\text{Mg}}^{\text{CC}}$ depends on the chosen AGB yield table, the AGB fraction, and the dataset. Additionally, these yields will be systematically biased if the galaxy is out of equilibrium, for example, due to a recent starburst (Mor et al. 2019; Isern 2019). Further exploration could investigate the magnitude of these uncertainties, but I find that the qualitative conclusions are similar despite substantial variations in the assumptions here.

4. The Multizone Model

Classical, *one-zone* models of chemical evolution assume instantaneous mixing of metals in the star-forming interstellar medium (e.g. Matteucci 2021). This simple framework is a poor approximation of the Milky Way. The Galaxy evolves *insideout*—where star formation is higher towards the center and in the early universe (Bird et al. 2013). Additionally, stars can migrate several kpcs over their lifetimes, mixing different chemical environments across the galaxy (Bird et al. 2012; Sellwood & Binney 2002). For the rest of this paper, I focus on multi-zone models, which discretize the Galaxy into concentric rings in which stars move between. Specifically, I make use of the Johnson et al. (2021) (hereafter J21) model for the Milky Way, which runs using the publicly available Versatile Integrator for Chemical Evolution (VICE). This model is described extensively in J21 and concisely summarized in Johnson et al. (2023). Here, I provide a brief overview of the relevant model components.

In the model, the Galaxy is divided into 200 rings, each 100 pc wide. Each ring has a separate stellar population and gas supply. Star formation ends beyond a radius $R = 15.5$ kpc. I initially assume an *insideout* SFH, where the star formation surface density Σ_\star is given by

$$\dot{\Sigma}_\star \propto \left(1 - e^{-t/\tau_{\text{rise}}}\right) e^{-t/\tau_{\text{sff}}}. \quad (14)$$

$\tau_{\text{rise}} = 2$ Gyr describes when the star formation rate reaches a maximum, and τ_{sff} describes the decay timescale of star formation as a function of radius R . J21 derives $\tau_{\text{sff}}(R)$ through analysis of four integral field spectroscopy surveys in Sánchez (2020). The star formation history is normalized such that the total stellar mass reaches $5.17 \times 10^{10} M_\odot$ (Licquia & Newman 2015) and at each R to match the stellar surface density gradient (Bland-Hawthorn & Gerhard 2016). The gas inflow is calculated to maintain our chosen SFH for each radius and time, using an

extension of a Kennicutt-Schmidt law (Kennicutt 1998),

$$\dot{\Sigma}_{\star} \propto \begin{cases} \Sigma_{\text{gas}} & 2 \times 10^7 \leq \Sigma_{\text{gas}} \\ (\Sigma_{\text{gas}})^{3.6} & 5 \times 10^6 \leq \Sigma_{\text{gas}} < 2 \times 10^7 \\ (\Sigma_{\text{gas}})^{1.7} & \Sigma_{\text{gas}} < 5 \times 10^6 \end{cases} \quad (15)$$

The scaling of this relationship varies with time due to the redshift dependence of τ_{\star} in molecular gas observed by Tacconi et al. (2018). I assume a Kroupa (2001) IMF.

J21 accounts for radial migration by using the results of the h277 hydrodynamical simulation (Christensen et al. 2012; Zolotov et al. 2012; Loebman et al. 2012; Brooks & Zolotov 2014), with simulation parameters described in Bird et al. (2021). Each VICE single stellar population (ssp) is matched to an *analog* in H277, chosen to form at a similar time and radius R . By taking the change in radius ΔR of the analogs, the ssp move to their final radii with a $\sqrt{\text{time}}$ dependence. This relationship between displacement and time arises when migration proceeds as a consequence of the diffusion of angular momentum (Frankel et al. 2018, 2020). I do not account for radial gas flows. Using the results of a hydrodynamical simulation without modification limits the free parameters in the model; however, I am limited to one dynamical history. The impact of the details of a galaxy’s dynamical history on its chemical evolution is still unknown.

As the strength of outflows controls the resulting α abundances, J21 create a metallicity gradient by defining

$$\eta(R) = \frac{y_{\alpha}^{\text{CC}}}{Z_{\alpha, \odot}} 10^{(-0.08 \text{ kpc}^{-1})(R-4 \text{ kpc})+0.3} + r - 1. \quad (16)$$

This choice of $\eta(R)$ results in a $[\alpha/\text{H}]$ gradient consistent with Milky Way observations (e.g. Hayden et al. 2014; Weinberg et al. 2019; Frinchaboy et al. 2013).

5. Multizone Model Results

5.1 Data Selection

Johnson et al. (2023) compare their model against the Vincenzo et al. (2021) sample of APOGEE (Majewski et al. 2017) red giant branch stars. Vincenzo et al. (2021) use MESA stellar evolution models (Paxton et al. 2011) to correct for the effects of first dredge up. I instead use the Roberts et al. (2023, in prep.) sample of APOGEE subgiants. Subgiant stars have not undergone first dredge up but have well-mixed atmospheres, so their atmospheric C and N abundances are still reflective of their birth abundances and do not need mixing corrections. I only compare the models to the low- α sequence unless otherwise specified. The selection criteria and differences between the samples are described in more detail in Appendix A.

5.2 The Evolution of Carbon Abundances in the Galaxy

Here, I present the time evolution of our fiducial model. In the next Sections, I will discuss the choice of parameters and agreement with observations. The fiducial model has the following qualitative characteristics of its C yields: (a) C is predominantly produced in CCSNE, (b) CCSNE produce more C at higher metallicities, and (c) AGB stars produce less C at higher metallicities. The fiducial model uses the C11 AGB yield tables (see Section 2.1, and Table 1), and I amplify the C11 yields by a factor of 2.9 such that AGB stars account for 20% of C at $Z = Z_{\odot}$.

I show the time evolution tracks of the fiducial model in Fig. 7 for $[C/Mg]$ - $[Mg/H]$ and $[C/Mg]$ - $[Mg/Fe]$. Comparing $[C/Mg]$ against $[Mg/Fe]$ enables us to see the late-time evolution of C more clearly. Because of the extended delay time distribution of SNE IA enrichment, $[Fe/H]$ takes longer to reach equilibrium, and the late-time evolution is not as clustered as $[Mg/H]$. The evolution proceeds as follows. Initially, CCSNE dominate production. As y_C^{CC} has strong metallicity dependence, $[C/Mg]$ increases with time. Shortly thereafter, AGB stars contribute delayed C, increasing $[C/Mg]$ even more steeply. As Mg begins to reach equilibrium, the

[C/Mg] ratio plateaus as C approaches equilibrium. Finally, as y_C^{AGB} decreases or even becomes negative with higher metallicity, the [C/Mg] abundance may decline slightly. This is more evident in the lower panel of Fig. 7—while the [C/Mg]-[Mg/H] trend reaches equilibrium at ~ 5 Gyr, the [C/Mg]-[Mg/Fe] trend continues to evolve even until the present day, exposing the effect of the relative delay times of AGB stars and SNE IA.

5.3 Low and High-Mass Stellar Yields

To parameterize the AGB contribution to C production, I define

$$f_{\text{AGB}} \equiv \frac{y_C^{\text{AGB}}}{y_C} \bigg|_{Z=Z_\odot}, \quad (17)$$

where y_C^{AGB} includes the multiplicative factor α_{AGB} as defined in Eq. 12. Fig. 8 compares the K10, K16, C11, and V13 yield models. I use the published, unscaled yield tables ($\alpha_{\text{AGB}} = 1$) for Fig. 8. As the highest AGB yield at solar, K10 is only $y_C^{\text{AGB}} = 0.000585$, $f_{\text{AGB}} \leq 0.12$ for all models. Massive stars dominate C production with unscaled yields. While it is easy to modify the AGB yields in my model, their small contribution reduces the effect. I leave a more detailed discussion of the effects of AGB models for Appendix C and use C11 yields hereafter.

Next, I investigate adjustments to the AGB yield fraction f_{AGB} and the CCSNE metallicity dependence ζ in Fig. 9. On the top panel of Fig. 9, I plot models with varying y_C^{CC} metallicity dependence. As discussed in Section 3, the [C/Mg]-[Mg/H] trend is approximated by equilibrium, so the trends of these have steeper [C/Mg]-[Mg/H] corresponding to steeper metallicity dependence. However, [C/Mg]-[Mg/Fe] is minimally affected by these changes since CCSNE occurs on much shorter timescales than SNE IA and AGB enrichment.

In the bottom panel of Fig. 9, I plot three models with different AGB fractions while using C11 yields. The [C/Mg]-[Mg/Fe] relationship is set by f_{AGB} because a specific amount of C must be released at a delayed time to match the SNE IA production of Fe and increase [C/Mg] as [Mg/Fe] decreases to reproduce the data. Increased f_{AGB} results in a decreased slope in [C/Mg]-[Mg/H], owing to the negative metallicity dependence of y_C^{AGB} . So while [C/Mg]-[Mg/H] alone cannot differentiate models which vary f_{AGB} and ζ correspondingly, [C/Mg]-[Mg/Fe] provides information on f_{AGB} . So, I can use [C/Mg]-[Mg/Fe] to estimate $f_{\text{AGB}} \approx 0.2$, and then choose ζ to match [C/Mg]-[Mg/H].

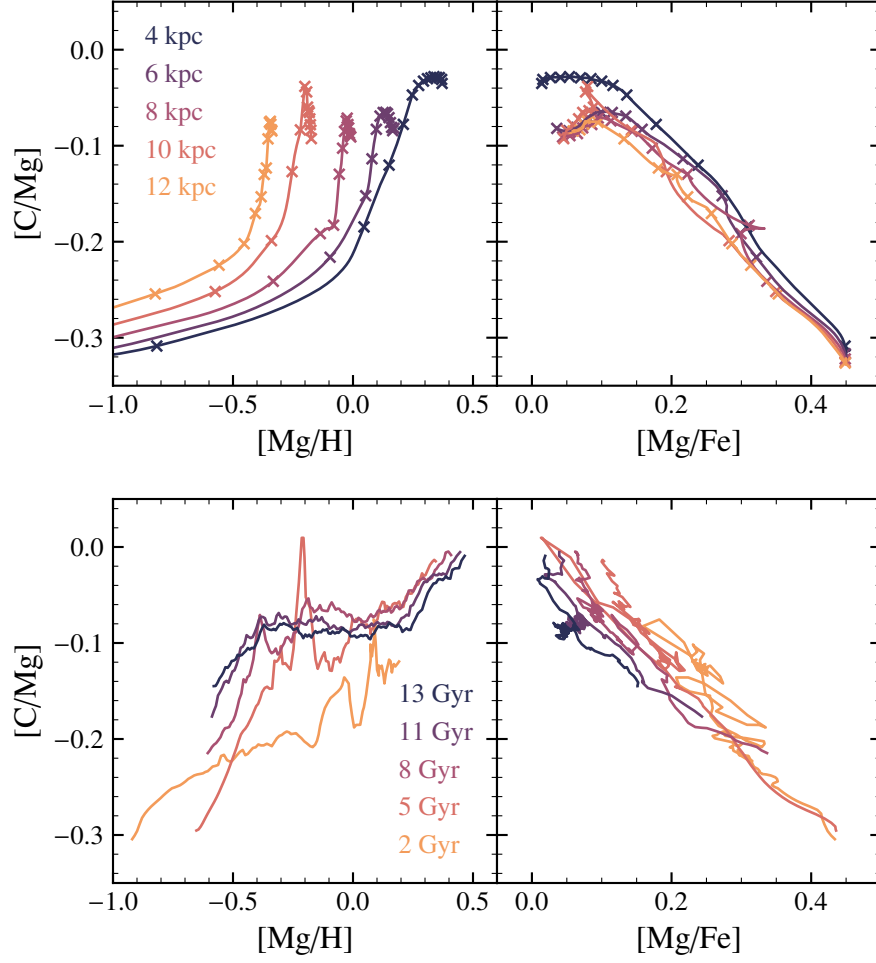


Figure 7: Time evolution of gas-phase C abundances in our fiducial model. **Top:** Evolutionary tracks parameterized by time at fixed Galactocentric radius in the [C/Mg]-[Mg/H] and [C/Mg]-[Mg/Fe] planes. **Bottom:** Snapshots of the gas-phase [C/Mg]-[Mg/H] and [C/Mg]-[Mg/Fe] trend, parameterized by radius at a fixed time.

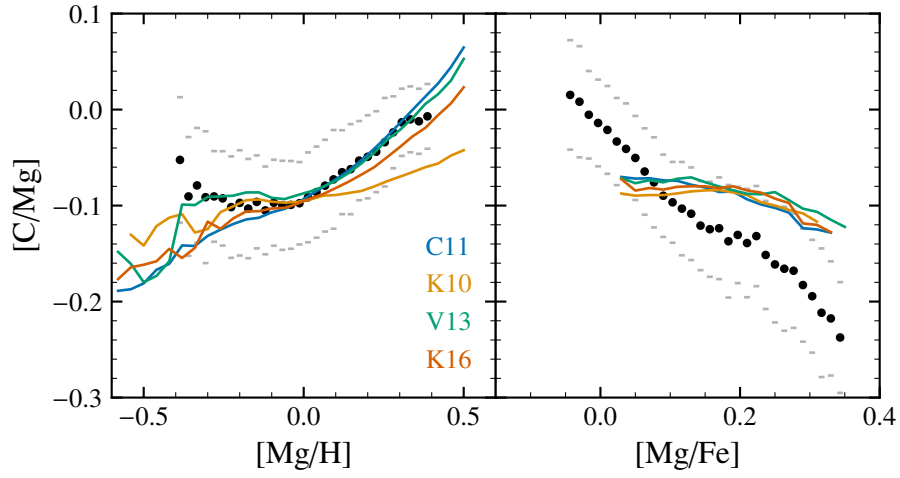


Figure 8: Stellar abundance trends in our model, assuming metallicity independent y_C^{CC} . Colored lines quantify the median $[C/Mg]$ in bins of $[Mg/H]$ for our four AGB yield models from the literature (see Section 2.1). Black points and grey dashes represent the median and standard deviations of $[C/Mg]$ for each $[Mg/H]$ bin in the Roberts et al. (2023, in prep.) sample. In the right panel, I show the trends only for stars where $-0.15 \leq [Mg/H] \leq -0.05$.

Table 2: For each AGB yield set, the IMF-averaged AGB C yield at solar metallicity $y_{\text{C},0}^{\text{AGB}}$ and the multiplicative factor reaches an AGB contribution of 20% $\alpha_{\text{AGB},20}$.

AGB Model	$y_{\text{C},0}^{\text{AGB}}$	$\alpha_{\text{AGB},20}$
C11	0.000347	2.9
K10	0.000585	1.7
V13	0.000060	16.5
K16	0.000421	2.4

One source of theoretical uncertainty in this result is that the SNE Ia yield and delay time distributions have their own uncertainties. I discuss variations in $y_{\text{Fe}}^{\text{Ia}}$ in Appendix C, and find that the qualitative conclusions are largely unaffected. I, therefore, focus on the choices of $y_{\text{Fe}}^{\text{Ia}} = 0.00214$ and a $t^{-1.1}$ delay time distribution choices from the fiducial model here. In short, the scaling of the trend and metallicity dependence of C (as seen in the [C/Mg]-[Mg/H] trend) gives information on the total C yield and the behavior of CCSNE (as the dominating producer of C), the [C/Mg]-[Mg/Fe] trend exposes the delayed effect of C from AGB contribution.

5.4 Star Formation History

Here, I consider a *lateburst* model, created by multiplying our fiducial *insideout* SFH with a Gaussian.

$$\dot{\Sigma}_{\text{lateburst}} \propto \dot{\Sigma}_{\text{insideout}} \left(1 + A e^{-(t-\tau_{\text{burst}})^2/2\sigma_{\text{burst}}^2} \right) \quad (18)$$

$A = 1.5$ represents the amplitude of the birth, $\tau_{\text{burst}} = 10.8 \text{ Gyr}$ is the time where the burst is strongest, and $\sigma_{\text{burst}} = 1 \text{ Gyr}$ is the width of the burst. I also consider an *earlyburst* model as a slight variation of the lateburst, where the burst is instead exponential and placed at $t_1 = 5 \text{ Gyr}$.

$$\dot{\Sigma}_{\text{earlyburst}} \propto \dot{\Sigma}_{\text{insideout}} + \begin{cases} A e^{-(t-t_1)/\tau_{\text{burst}}} & t_1 < t \\ 0 & t < t_1 \end{cases} \quad (19)$$

where I take the burst duration, $\tau_{\text{burst}} = 1 \text{ Gyr}$ in this case. This approximately corresponds to the Gaia-Encelidus merger, inducing higher star formation in the Milky Way (Spitoni et al. 2021; Bonaca et al. 2020; Helmi et al. 2018).

Fig. 10 shows three models with these alternate SFH. Changes to the SFH leave [C/Mg]-[Mg/H] unchanged, but they do introduce slight variation in [C/Mg]-[Mg/Fe]. Models with higher AGB fractions are more sensitive to variations in the

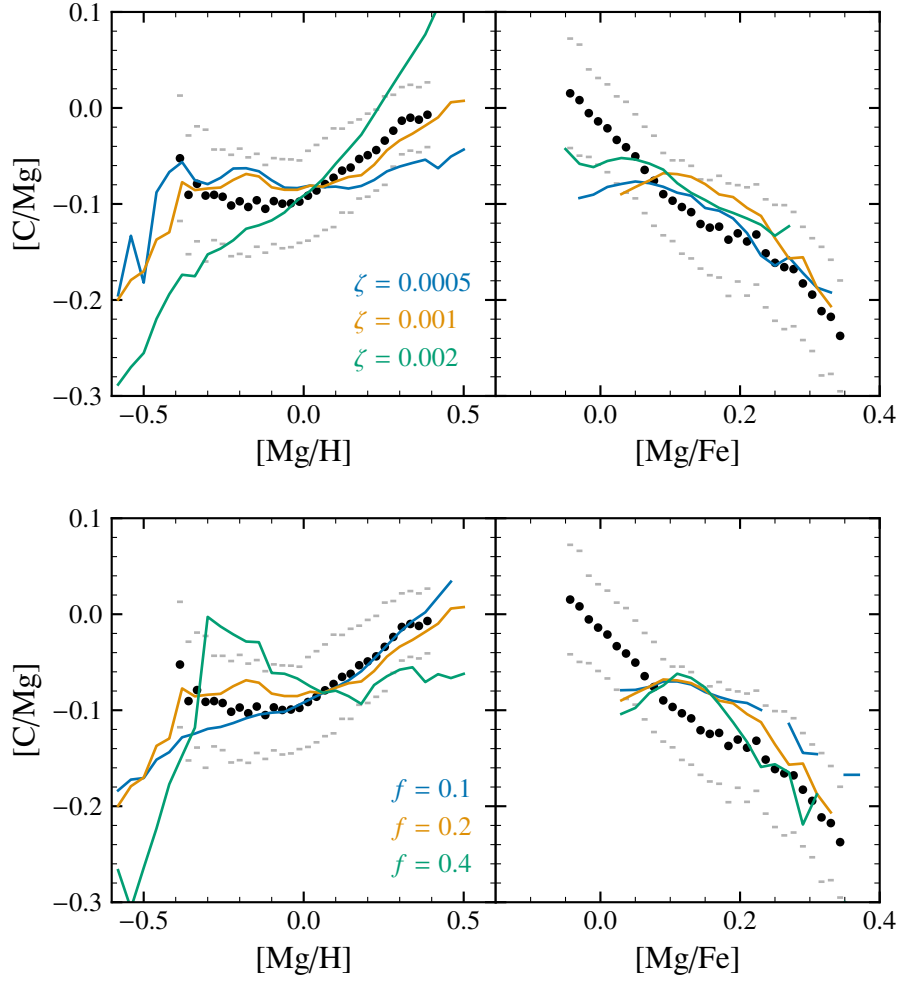


Figure 9: Similar to Fig. 8 except the top plot shows the fiducial model with lower and higher values of ζ , the metallicity dependence of y_C^{CC} . The bottom plot shows models with $f_{AGB} = 0.1, 0.2$, and 0.4 . Both the f_{AGB} and ζ influence $[C/Mg]$ - $[Mg/H]$, but only f_{AGB} has a significant impact on $[C/Mg]$ - $[Mg/Fe]$.

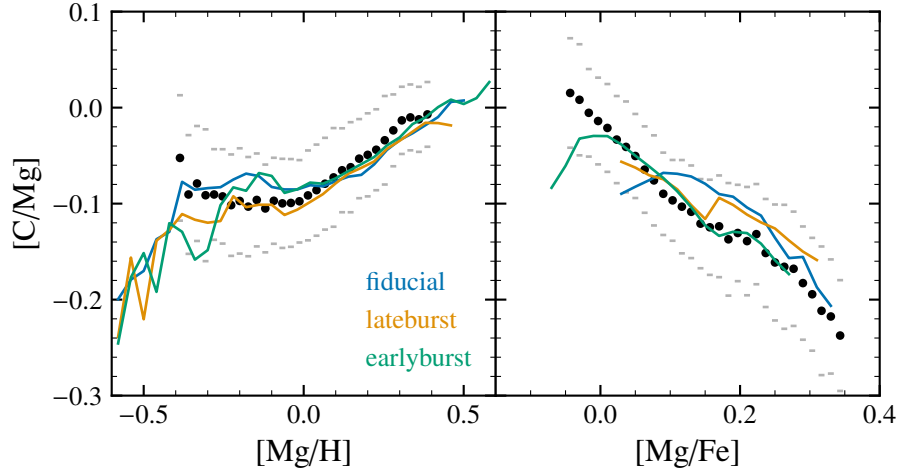


Figure 10: Similar to Fig. 8 but comparing the fiducial model to alternate SFHS (see Section 5.4).

SFH. The late burst models result in $[C/Mg]$ continuing to increase at low $[Mg/Fe]$, but also introduce a dip not present in the data. Additionally, the early burst reproduces the slight break between the low and high α sequences, but overshoots equilibrium more severely than the fiducial model. In general, any of these SFHS are consistent with this model.

5.5 Outflows

GCE models of the Milky Way fall into two classes—those which incorporate significant mass-loading (e.g., this work) and those which neglect mass-loading but lower effective yield to match observed abundances (e.g. Minchev et al. 2013, 2014; Spitoni et al. 2019, 2020, 2021). An increase in stellar yields has a nearly identical effect as a decrease in the mass-loading factor η (see Appendix B of Johnson et al. 2022). The equilibrium arguments discussed in Section 3 suggest however that abundance ratios are independent of the choice of normalization and the value of η . I, therefore, expect my results regarding the relative yield y_C/y_{Mg} and its metallicity dependence to extend to the other class of models omitting mass loading. I demonstrate this further here.

The theoretical motivation for decreasing yields is the uncertainty in stellar explodability. If fewer high-mass stars explode, then the yields will be reduced by

some factor. Additionally, some fraction of supernovae ejecta may be lost directly to an outflow, lowering effective yields. To explore reduced outflow models, I lower both η and all yields by the same factor to leave the equilibrium abundances unchanged.

Fig. 11 shows models with variations of the mass loading strength. While changing the value of η affects the metallicity distribution of stars, all of the models in Fig. 11 still evolve along the same path. My model is unable to differentiate a uniform decrease in both outflows and yields.

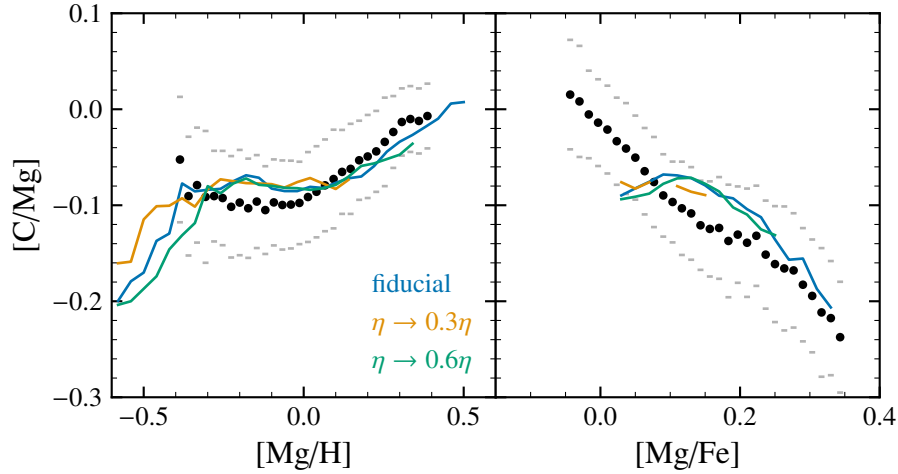


Figure 11: Similar to Fig. 8 but comparing the fiducial model to reduced mass loading models (see Section 5.5). Both yields and mass-loading are adjusted correspondingly such that the equilibrium abundances are unchanged.

5.6 Scatter

Median trends have limitations as they do not consider the actual distribution of $[C/Mg]$ - $[Mg/H]$ abundances. So, Fig. 12 compares the predicted distribution of the model to contours of the subgiant sample. The model reproduces this 2-dimension distribution well when including scatter based on the median APOGEE abundance errors for each metallicity bin. Some scatter is due to radial migration, but observational errors are dominant. Precision abundance measurements will allow tighter constraints on relative yields.

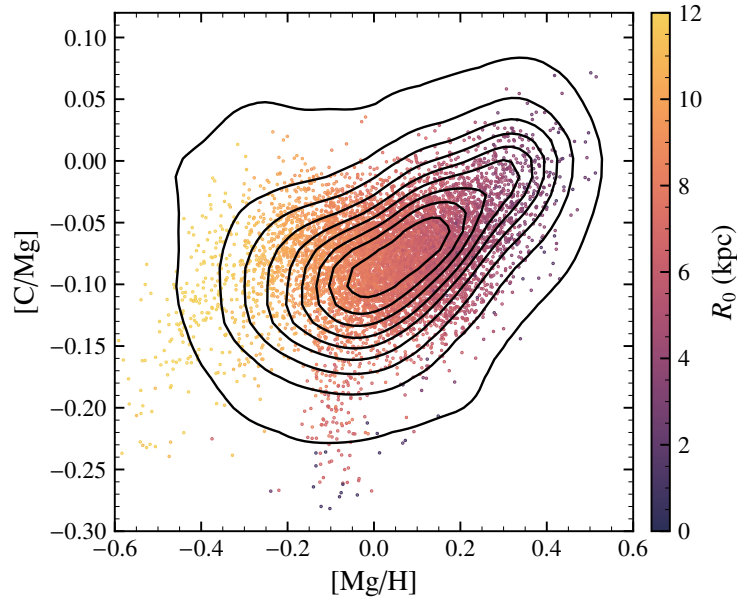


Figure 12: The stars in the fiducial model in the $[C/Mg]$ - $[Mg/H]$ plane compared to contours of the subgiant sample. I add random noise to the scatter points equal to the median uncertainties in the subgiant sample. Stars are color-coded such that lighter colors represent populations born at greater galactocentric radii. The plot only includes low- α stars.

5.7 Gas-Phase Abundances

As an additional test of the model, I next compare the model predictions against gas-phase measurements. Fig. 14 shows the fiducial model’s gas-phase predictions compared to observations of the Milky Way and extragalactic HII regions, halo stars, and DLA systems. The model is broadly consistent with observations, where the model at $t = 2$ Gyr approximates the slope of dwarf galaxies and halo stars. The increase of C/O at higher metallicities is also consistent with the high C/O abundances measured in extragalactic HII regions. My model does not extend to very low metallicity, where the slope of the trend inverts, but broadly explains observations above $[\text{O}/\text{H}] \gtrsim -1$.

Mg measurements are more reliable, but O abundances are easier to measure in HII regions. So while I use Mg as the representative α -element for stellar abundances, I instead use O when comparing gas-phase abundances. As I assume $[\text{Mg}/\text{O}] = 0$, my model is independent of the choice of the α -element

Measurements of C abundances in the gas-phase are challenging. In HII regions, C/O abundance ratios are measured with either recombination lines or collisional excitation lines. However C lacks strong collisional excitation lines, and recombination lines fall in the ultraviolet without nearby reference H lines (Skillman et al. 2020). Additionally, recombination and collisional excitation measurements disagree by a factor of ~ 2 (García-Rojas & Esteban 2007). Variations in the SFHS may furthermore increase scatter, as AGB are a delayed source of C.

The decreasing $[\text{C}/\text{O}]$ abundance at very-low metallicities is likely due to population III stellar yields (e.g. Hirschi 2007), as suggested by Cooke et al. (2017) and Frebel & Norris (2015). AGB stars cannot explain the increase in C yields at low metallicity in the DLA sample as the evolutionary timescales of DLAs are shorter than the typical delay time distribution of AGB stars.

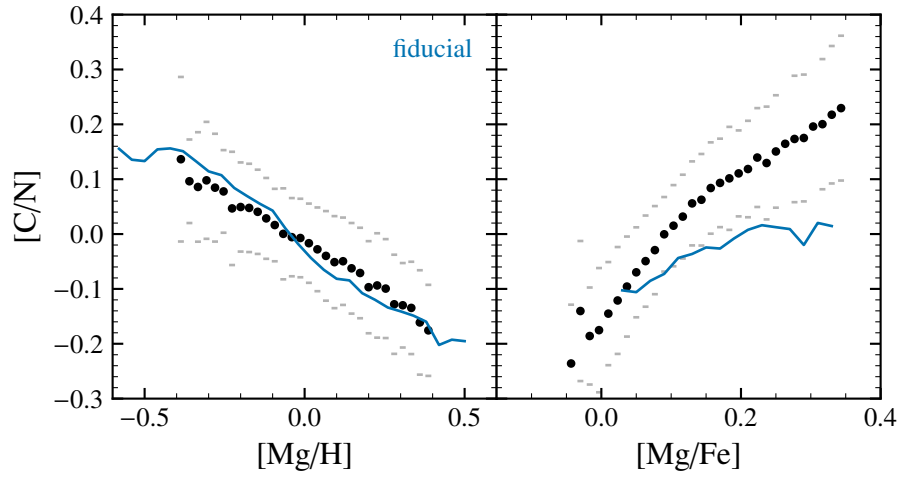


Figure 13: Similar to Fig. 8, except comparing $[C/N]$ from the fiducial model only. N yields are adapted from Johnson et al. (2023). (See also Table 1.)

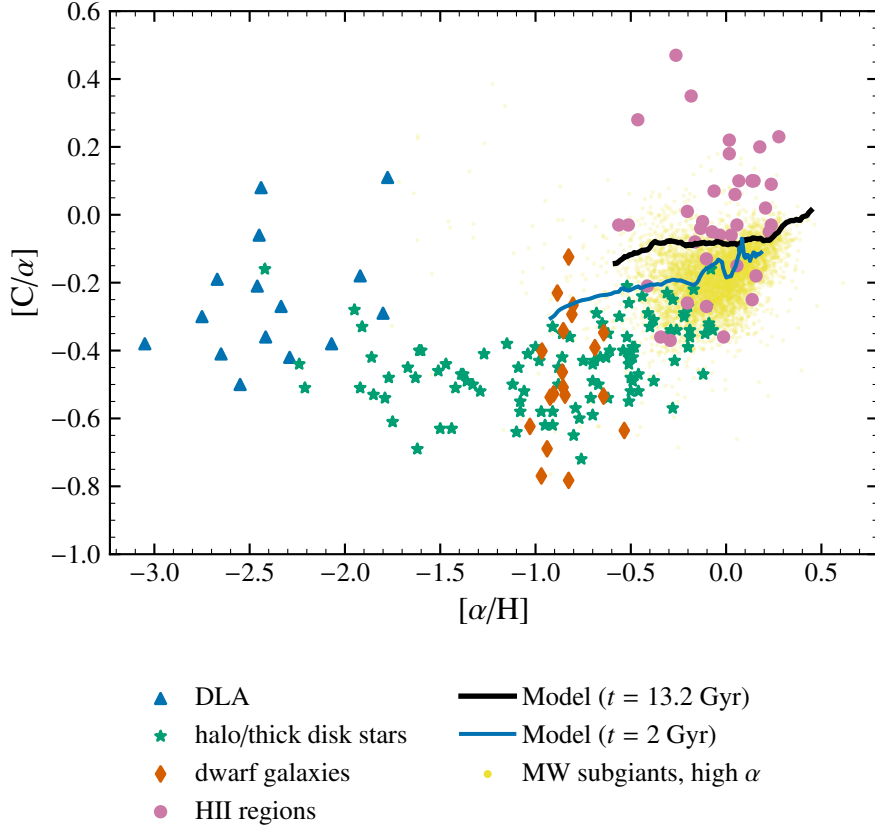


Figure 14: Gas-phase C abundances. We plot our model at $t = 2$ Gyr and present day as thick solid lines. Points represent measurements in HII regions (pink circles; Skillman et al. 2020; Esteban et al. 2002, 2009, 2014, 2019) DLA systems (blue triangles; Ellison et al. 2010; Srianand et al. 2010; Dutta et al. 2014; Dessauges-Zavadsky et al. 2003; Pettini et al. 2008; Morrison et al. 2016; Cooke et al. 2017), dwarf galaxies (red diamonds; Berg et al. 2019), Milky Way halo and thick disk stars (green stars; Nissen et al. 2014; Fabbian et al. 2009), and Milky Way high- α stars (yellow points; Robert et al. 2023, in prep.).

6. Conclusions

In this work, I investigate the role of C yields on the predictions of multi-zone GCE models. Johnson et al. (2023) performed a similar analysis focusing on N. They found that matching the observed relationship between N and O abundances¹ requires relative N and O yields from simple stellar populations with a roughly linear dependence on metallicity (i.e. $y_N/y_O \propto Z$). Here, I perform a similar analysis on C.

Though CCSNE C yields are poorly understood, I adopt an equilibrium approximation and determine a functional form that approximately matches trends in APOGEE subgiant and is consistent with high-mass star nucleosynthesis models. Variations of the metallicity dependence of this CCSNE yield affect trends in [C/Mg]-[Mg/H] but do not affect trends in [C/Mg]-[Mg/Fe] (when taking a slice in [Mg/H]). As all theoretical AGB C yields decrease with metallicity, increasing the AGB fraction causes the [C/Mg]-[Mg/H] trend to flatten. However, the [C/Mg]-[Mg/Fe] trend is sensitive to the AGB fraction. From this, I estimate that AGB stars contribute $\sim 20\%$ of total C abundance at solar metallicity. The remaining $\sim 80\%$ of C comes from high-mass star with a metallicity dependent yield of $y_C^{\text{CC}}/y_{\text{Mg}}^{\text{CC}} = 1.51 + 0.54(Z/Z_\odot)$. This metallicity dependence is roughly consistent with rotating stellar yields.

I additionally explore variations of the assumed SFH and outflow mass-loading factor η . I find that alternate SFHs can slightly affect [C/Mg]-[Mg/Fe], but [C/Mg]-[Mg/H] is mostly unaffected. Decreasing both outflows and yields by the same factor leaves the [C/Mg]-[Mg/H] and [C/Mg]-[Mg/Fe] trends unaffected. These constraints on the relative yields of C, O, and Mg are robust against variations in η .

Finally, I compare my model against gas-phase measurements and metal-poor stars. While my model was built on data near solar metallicity, observations of very low metallicity, high redshift damped Lyman- α systems indicate higher C/O ratios (Cooke et al. 2017), consistent with yields from population III stars (e.g. Hirschi 2007). Population III stars, CCSNE and AGBstars altogether explain the observed

¹e.g. Henry et al. (2000); Pilyugin et al. (2010); Berg et al. (2012, 2020); Skillman et al. (2020); Izotov et al. (2012); James et al. (2015); Dopita et al. (2016).

evolutionary history of C.

These C yield constraints provide a useful benchmark for stellar evolution models. C yields are sensitive to poorly understood processes, including mass-loss prescriptions, explodability, nuclear cross sections, convection, and stellar structure. Future spectroscopic surveys combined with Gaia kinematics (Gaia Collaboration et al. 2016) will continue to enhance our understanding of chemical evolution. Both the Sloan Digital Sky Survey V's Milky Way Mapper program (SDSS-V/MWM) (Kollmeier et al. 2017) and the Dark Energy Spectroscopic Instrument (DESI) Milky Way survey (DESI Collaboration et al. 2016; Cooper et al. 2022) will each measure spectra of upwards 6,000,000 Milky Way stars. These larger samples will enable similar work to tighten constraints on stellar models and our understanding of galaxy structure and evolution.

Bibliography

- Abdurro'uf, Accetta, K., Aerts, C., et al. 2022, *ApJS*, 259, 35, doi: 10.3847/1538-4365/ac4414
- Adelberger, E. G., García, A., Robertson, R. G. H., et al. 2011, *Reviews of Modern Physics*, 83, 195, doi: 10.1103/RevModPhys.83.195
- Asplund, M., Grevesse, N., Sauval, A. J., & Scott, P. 2009, *ARA&A*, 47, 481, doi: 10.1146/annurev.astro.46.060407.145222
- Astropy Collaboration, Robitaille, T. P., Tollerud, E. J., et al. 2013, *A&A*, 558, A33, doi: 10.1051/0004-6361/201322068
- Astropy Collaboration, Price-Whelan, A. M., Sipőcz, B. M., et al. 2018, *AJ*, 156, 123, doi: 10.3847/1538-3881/aabc4f
- Astropy Collaboration, Price-Whelan, A. M., Lim, P. L., et al. 2022, *ApJ*, 935, 167, doi: 10.3847/1538-4357/ac7c74
- Berg, D. A., Erb, D. K., Henry, R. B. C., Skillman, E. D., & McQuinn, K. B. W. 2019, *ApJ*, 874, 93, doi: 10.3847/1538-4357/ab020a
- Berg, D. A., Pogge, R. W., Skillman, E. D., et al. 2020, *ApJ*, 893, 96, doi: 10.3847/1538-4357/ab7eab
- Berg, D. A., Skillman, E. D., Marble, A. R., et al. 2012, *ApJ*, 754, 98, doi: 10.1088/0004-637X/754/2/98
- Bird, J. C., Kazantzidis, S., & Weinberg, D. H. 2012, *MNRAS*, 420, 913, doi: 10.1111/j.1365-2966.2011.19728.x
- Bird, J. C., Kazantzidis, S., Weinberg, D. H., et al. 2013, *ApJ*, 773, 43, doi: 10.1088/0004-637X/773/1/43

- Bird, J. C., Loebman, S. R., Weinberg, D. H., et al. 2021, MNRAS, 503, 1815, doi: 10.1093/mnras/stab289
- Bland-Hawthorn, J., & Gerhard, O. 2016, ARA&A, 54, 529, doi: 10.1146/annurev-astro-081915-023441
- Bonaca, A., Conroy, C., Cargile, P. A., et al. 2020, ApJ, 897, L18, doi: 10.3847/2041-8213/ab9caa
- Brooks, A. M., & Zolotov, A. 2014, ApJ, 786, 87, doi: 10.1088/0004-637X/786/2/87
- Christensen, C., Quinn, T., Governato, F., et al. 2012, MNRAS, 425, 3058, doi: 10.1111/j.1365-2966.2012.21628.x
- Cooke, R. J., Pettini, M., & Steidel, C. C. 2017, MNRAS, 467, 802, doi: 10.1093/mnras/stx037
- Cooper, A. P., Koposov, S. E., Allende Prieto, C., et al. 2022, arXiv e-prints, arXiv:2208.08514, doi: 10.48550/arXiv.2208.08514
- Cristallo, S., Straniero, O., Piersanti, L., & Gobrecht, D. 2015, ApJS, 219, 40, doi: 10.1088/0067-0049/219/2/40
- Cristallo, S., Piersanti, L., Straniero, O., et al. 2011, ApJS, 197, 17, doi: 10.1088/0067-0049/197/2/17
- Dalcanton, J. J. 2007, ApJ, 658, 941, doi: 10.1086/508913
- DESI Collaboration, Aghamousa, A., Aguilar, J., et al. 2016, arXiv e-prints, arXiv:1611.00036, doi: 10.48550/arXiv.1611.00036
- Dessauges-Zavadsky, M., Péroux, C., Kim, T. S., D’Odorico, S., & McMahon, R. G. 2003, MNRAS, 345, 447, doi: 10.1046/j.1365-8711.2003.06949.x
- Dopita, M. A., Kewley, L. J., Sutherland, R. S., & Nicholls, D. C. 2016, Ap&SS, 361, 61, doi: 10.1007/s10509-016-2657-8
- Dutta, R., Srianand, R., Rahmani, H., et al. 2014, MNRAS, 440, 307, doi: 10.1093/mnras/stu260
- Ellison, S. L., Prochaska, J. X., Hennawi, J., et al. 2010, MNRAS, 406, 1435, doi: 10.1111/j.1365-2966.2010.16780.x

- Esteban, C., Bresolin, F., Peimbert, M., et al. 2009, *ApJ*, 700, 654, doi: 10.1088/0004-637X/700/1/654
- Esteban, C., García-Rojas, J., Arellano-Córdova, K. Z., & Méndez-Delgado, J. E. 2019, arXiv e-prints, arXiv:1905.10129. <https://arxiv.org/abs/1905.10129>
- Esteban, C., García-Rojas, J., Carigi, L., et al. 2014, *MNRAS*, 443, 624, doi: 10.1093/mnras/stu1177
- Esteban, C., Peimbert, M., Torres-Peimbert, S., & Rodríguez, M. 2002, *ApJ*, 581, 241, doi: 10.1086/344104
- Fabbian, D., Nissen, P. E., Asplund, M., Pettini, M., & Akerman, C. 2009, *A&A*, 500, 1143, doi: 10.1051/0004-6361/200810095
- Finlator, K., & Davé, R. 2008, *MNRAS*, 385, 2181, doi: 10.1111/j.1365-2966.2008.12991.x
- Frankel, N., Rix, H.-W., Ting, Y.-S., Ness, M., & Hogg, D. W. 2018, *ApJ*, 865, 96, doi: 10.3847/1538-4357/aadba5
- Frankel, N., Sanders, J., Ting, Y.-S., & Rix, H.-W. 2020, *ApJ*, 896, 15, doi: 10.3847/1538-4357/ab910c
- Frebel, A., & Norris, J. E. 2015, *ARA&A*, 53, 631, doi: 10.1146/annurev-astro-082214-122423
- Frinchaboy, P. M., Thompson, B., Jackson, K. M., et al. 2013, *ApJ*, 777, L1, doi: 10.1088/2041-8205/777/1/L1
- Gaia Collaboration, Prusti, T., de Bruijne, J. H. J., et al. 2016, *A&A*, 595, A1, doi: 10.1051/0004-6361/201629272
- García Pérez, A. E., Allende Prieto, C., Holtzman, J. A., et al. 2016, *AJ*, 151, 144, doi: 10.3847/0004-6256/151/6/144
- García-Rojas, J., & Esteban, C. 2007, *ApJ*, 670, 457, doi: 10.1086/521871
- Gilroy, K. K. 1989, *ApJ*, 347, 835, doi: 10.1086/168173
- Griffith, E. J., Sukhbold, T., Weinberg, D. H., et al. 2021, *ApJ*, 921, 73, doi: 10.3847/1538-4357/ac1bac

- Harris, C. R., Millman, K. J., van der Walt, S. J., et al. 2020, *Nature*, 585, 357, doi: 10.1038/s41586-020-2649-2
- Hasselquist, S., Holtzman, J. A., Shetrone, M., et al. 2019, *ApJ*, 871, 181, doi: 10.3847/1538-4357/aaf859
- Hayden, M. R., Holtzman, J. A., Bovy, J., et al. 2014, *AJ*, 147, 116, doi: 10.1088/0004-6256/147/5/116
- Helmi, A., Babusiaux, C., Koppelman, H. H., et al. 2018, *Nature*, 563, 85, doi: 10.1038/s41586-018-0625-x
- Henry, R. B. C., Edmunds, M. G., & Köppen, J. 2000, *ApJ*, 541, 660, doi: 10.1086/309471
- Hirschi, R. 2007, *A&A*, 461, 571, doi: 10.1051/0004-6361:20065356
- Hunter, J. D. 2007, *Computing in Science & Engineering*, 9, 90, doi: 10.1109/MCSE.2007.55
- Iben, Icko, J. 1967, *ARA&A*, 5, 571, doi: 10.1146/annurev.aa.05.090167.003035
- Isern, J. 2019, *ApJ*, 878, L11, doi: 10.3847/2041-8213/ab238e
- Izotov, Y. I., Thuan, T. X., & Guseva, N. G. 2012, *A&A*, 546, A122, doi: 10.1051/0004-6361/201219733
- James, B. L., Koposov, S., Stark, D. P., et al. 2015, *MNRAS*, 448, 2687, doi: 10.1093/mnras/stv175
- Johnson, J. A. 2019, *Science*, 363, 474, doi: 10.1126/science.aau9540
- Johnson, J. W., & Weinberg, D. H. 2020, *MNRAS*, 498, 1364, doi: 10.1093/mnras/staa2431
- Johnson, J. W., Weinberg, D. H., Vincenzo, F., Bird, J. C., & Griffith, E. J. 2023, *MNRAS*, 520, 782, doi: 10.1093/mnras/stad057
- Johnson, J. W., Weinberg, D. H., Vincenzo, F., et al. 2021, *MNRAS*, 508, 4484, doi: 10.1093/mnras/stab2718
- Johnson, J. W., Conroy, C., Johnson, B. D., et al. 2022, *arXiv e-prints*, arXiv:2210.01816, doi: 10.48550/arXiv.2210.01816

- Karakas, A. I. 2010, MNRAS, 403, 1413, doi: 10.1111/j.1365-2966.2009.16198.x
- Karakas, A. I., & Lattanzio, J. C. 2014, PASA, 31, e030, doi: 10.1017/pasa.2014.21
- Karakas, A. I., & Lugaro, M. 2016, ApJ, 825, 26, doi: 10.3847/0004-637X/825/1/26
- Karakas, A. I., Lugaro, M., Carlos, M., et al. 2018, MNRAS, 477, 421, doi: 10.1093/mnras/sty625
- Kennicutt, Robert C., J. 1998, ARA&A, 36, 189, doi: 10.1146/annurev.astro.36.1.189
- Kollmeier, J. A., Zasowski, G., Rix, H.-W., et al. 2017, arXiv e-prints, arXiv:1711.03234, doi: 10.48550/arXiv.1711.03234
- Korn, A. J., Grundahl, F., Richard, O., et al. 2007, ApJ, 671, 402, doi: 10.1086/523098
- Kroupa, P. 2001, MNRAS, 322, 231, doi: 10.1046/j.1365-8711.2001.04022.x
- Laird, J. B. 1985, ApJ, 289, 556, doi: 10.1086/162916
- Lambert, D. L., Gustafsson, B., Eriksson, K., & Hinkle, K. H. 1986, ApJS, 62, 373, doi: 10.1086/191145
- Lambert, D. L., & Ries, L. M. 1981, ApJ, 248, 228, doi: 10.1086/159147
- Larson, R. B. 1972, Nature Physical Science, 236, 7, doi: 10.1038/physci236007a0
- . 1974, MNRAS, 166, 585, doi: 10.1093/mnras/166.3.585
- Licquia, T. C., & Newman, J. A. 2015, ApJ, 806, 96, doi: 10.1088/0004-637X/806/1/96
- Lilly, S. J., Carollo, C. M., Pipino, A., Renzini, A., & Peng, Y. 2013, ApJ, 772, 119, doi: 10.1088/0004-637X/772/2/119
- Limongi, M., & Chieffi, A. 2018, ApJS, 237, 13, doi: 10.3847/1538-4365/aacb24
- Lind, K., Korn, A. J., Barklem, P. S., & Grundahl, F. 2008, A&A, 490, 777, doi: 10.1051/0004-6361:200810051

- Loebman, S. R., Ivezić, Ž., Quinn, T. R., et al. 2012, *ApJ*, 758, L23, doi: 10.1088/2041-8205/758/1/L23
- Majewski, S. R., Schiavon, R. P., Frinchaboy, P. M., et al. 2017, *AJ*, 154, 94, doi: 10.3847/1538-3881/aa784d
- Maoz, D., Mannucci, F., & Brandt, T. D. 2012, *MNRAS*, 426, 3282, doi: 10.1111/j.1365-2966.2012.21871.x
- Martig, M., Fouesneau, M., Rix, H.-W., et al. 2016, *MNRAS*, 456, 3655, doi: 10.1093/mnras/stv2830
- Masseron, T., & Gilmore, G. 2015, *MNRAS*, 453, 1855, doi: 10.1093/mnras/stv1731
- Matteucci, F. 2021, *A&A Rev.*, 29, 5, doi: 10.1007/s00159-021-00133-8
- Minchev, I., Chiappini, C., & Martig, M. 2013, *A&A*, 558, A9, doi: 10.1051/0004-6361/201220189
- . 2014, *A&A*, 572, A92, doi: 10.1051/0004-6361/201423487
- Mor, R., Robin, A. C., Figueras, F., Roca-Fàbrega, S., & Luri, X. 2019, *A&A*, 624, L1, doi: 10.1051/0004-6361/201935105
- Morrison, S., Kulkarni, V. P., Som, D., et al. 2016, *ApJ*, 830, 158, doi: 10.3847/0004-637X/830/2/158
- Nissen, P. E., Chen, Y. Q., Carigi, L., Schuster, W. J., & Zhao, G. 2014, *A&A*, 568, A25, doi: 10.1051/0004-6361/201424184
- Nomoto, K., Kobayashi, C., & Tominaga, N. 2013, *ARA&A*, 51, 457, doi: 10.1146/annurev-astro-082812-140956
- Ohio Supercomputer Center. 1987, Ohio Supercomputer Center. <http://osc.edu/ark:/19495/f5s1ph73>
- Pagel, B. E. J. 2009, *Nucleosynthesis and Chemical Evolution of Galaxies*, 2nd edn. (Cambridge University Press), doi: 10.1017/CBO9780511812170
- pandas development team, T. 2020, pandas-dev/pandas: Pandas, latest, Zenodo, doi: 10.5281/zenodo.3509134

- Paxton, B., Bildsten, L., Dotter, A., et al. 2011, *ApJS*, 192, 3, doi: 10.1088/0067-0049/192/1/3
- Peeples, M. S., & Shankar, F. 2011, *MNRAS*, 417, 2962, doi: 10.1111/j.1365-2966.2011.19456.x
- Pérez, F., & Granger, B. E. 2007, *Computing in Science and Engineering*, 9, 21, doi: 10.1109/MCSE.2007.53
- Pettini, M., Zych, B. J., Steidel, C. C., & Chaffee, F. H. 2008, *MNRAS*, 385, 2011, doi: 10.1111/j.1365-2966.2008.12951.x
- Pilyugin, L. S., Vílchez, J. M., & Thuan, T. X. 2010, *ApJ*, 720, 1738, doi: 10.1088/0004-637X/720/2/1738
- Sánchez, S. F. 2020, *ARA&A*, 58, 99, doi: 10.1146/annurev-astro-012120-013326
- Sellwood, J. A., & Binney, J. J. 2002, *MNRAS*, 336, 785, doi: 10.1046/j.1365-8711.2002.05806.x
- Skillman, E. D., Berg, D. A., Pogge, R. W., et al. 2020, *ApJ*, 894, 138, doi: 10.3847/1538-4357/ab86ae
- Souto, D., Cunha, K., Smith, V. V., et al. 2018, *ApJ*, 857, 14, doi: 10.3847/1538-4357/aab612
- Souto, D., Allende Prieto, C., Cunha, K., et al. 2019, *ApJ*, 874, 97, doi: 10.3847/1538-4357/ab0b43
- Spitoni, E., Silva Aguirre, V., Matteucci, F., Calura, F., & Grisoni, V. 2019, *A&A*, 623, A60, doi: 10.1051/0004-6361/201834188
- Spitoni, E., Verma, K., Silva Aguirre, V., & Calura, F. 2020, *A&A*, 635, A58, doi: 10.1051/0004-6361/201937275
- Spitoni, E., Verma, K., Silva Aguirre, V., et al. 2021, *A&A*, 647, A73, doi: 10.1051/0004-6361/202039864
- Srianand, R., Gupta, N., Petitjean, P., Noterdaeme, P., & Ledoux, C. 2010, *MNRAS*, 405, 1888, doi: 10.1111/j.1365-2966.2010.16574.x
- Sukhbold, T., Ertl, T., Woosley, S. E., Brown, J. M., & Janka, H. T. 2016, *ApJ*, 821, 38, doi: 10.3847/0004-637X/821/1/38

- Tacconi, L. J., Genzel, R., Saintonge, A., et al. 2018, *ApJ*, 853, 179, doi: 10.3847/1538-4357/aaa4b4
- Tinsley, B. M. 1980, *Fund. Cosmic Phys.*, 5, 287, doi: 10.48550/arXiv.2203.02041
- Ventura, P., Dell’Agli, F., Lugaro, M., et al. 2020, *A&A*, 641, A103, doi: 10.1051/0004-6361/202038289
- Ventura, P., Dell’Agli, F., Schneider, R., et al. 2014, *MNRAS*, 439, 977, doi: 10.1093/mnras/stu028
- Ventura, P., Di Criscienzo, M., Carini, R., & D’Antona, F. 2013, *MNRAS*, 431, 3642, doi: 10.1093/mnras/stt444
- Ventura, P., Karakas, A., Dell’Agli, F., García-Hernández, D. A., & Guzman-Ramirez, L. 2018, *MNRAS*, 475, 2282, doi: 10.1093/mnras/stx3338
- Vincenzo, F., Weinberg, D. H., Montalbán, J., et al. 2021, arXiv e-prints, arXiv:2106.03912. <https://arxiv.org/abs/2106.03912>
- Virtanen, P., Gommers, R., Oliphant, T. E., et al. 2020, *Nature Methods*, 17, 261, doi: 10.1038/s41592-019-0686-2
- Waskom, M. L. 2021, *Journal of Open Source Software*, 6, 3021, doi: 10.21105/joss.03021
- Weinberg, D. H., Andrews, B. H., & Freudenburg, J. 2017, *ApJ*, 837, 183, doi: 10.3847/1538-4357/837/2/183
- Weinberg, D. H., Holtzman, J. A., Hasselquist, S., et al. 2019, *ApJ*, 874, 102, doi: 10.3847/1538-4357/ab07c7
- Weinberg, D. H., Holtzman, J. A., Johnson, J. A., et al. 2022, *ApJS*, 260, 32, doi: 10.3847/1538-4365/ac6028
- Woosley, S. E., & Weaver, T. A. 1995, *ApJS*, 101, 181, doi: 10.1086/192237
- Zolotov, A., Brooks, A. M., Willman, B., et al. 2012, *ApJ*, 761, 71, doi: 10.1088/0004-637X/761/1/71

A. The Subgiant Sample

As the primary observational constraint, I use the criteria outlined in Roberts et al. (2023, in prep.) to create a sample of subgiants from APOGEE DR17 (Majewski et al. 2017). APOGEE is part of the Sloan Digital Sky Survey and measures high-resolution spectra of thousands of stars Abdurro’uf et al. (2022). Chemical abundances are determined from the APOGEE Stellar Parameter and Chemical Abundance Pipeline (ASPCAP) (García Pérez et al. 2016).

Photospheric C and N abundances in subgiants are reflective of their birth abundances (Gilroy 1989; Korn et al. 2007; Lind et al. 2008; Souto et al. 2018, 2019) As first dredge up, which affects C and N abundances, only occurs during the ascent onto the red giant branch, subgiant stars are unaffected by this enrichment.

An alternate approach for this analysis would be to estimate the birth abundances of red giant branch stars by correcting surface abundance effects from first dredge up as in Vincenzo et al. (2021). Subgiants are the more attractive option since these observations do not rely on model-dependent corrections. However, red giant branch stars are more luminous, potentially allowing better coverage of the Galactic disk.

I choose to use Roberts et al. (2023, in prep.) sample as this does not rely on additional layers of modeling, providing a more direct constraint to our model and limiting our systematic uncertainties.

Fig. 15 shows a plot of all APOGEE stars and the Roberts et al. (2023, in prep.) polygon selection criteria. Roberts et al. (2023, in prep.) select a region of stars based on surface gravity $\log g$, and effective surface temperature, T_{eff} .

$$\left\{ \begin{array}{l} \log g \geq 3.5 \\ \log g \leq 0.004 T_{\text{eff}} - 15.7 \\ \log g \leq 0.000706 T_{\text{eff}} + 0.36 \\ \log g \leq -0.0015 T_{\text{eff}} + 12.05 \\ \log g \geq 0.0012 T_{\text{eff}} - 2.8. \end{array} \right. \quad (20)$$

Additionally, I included stars in APOGEE marked by the following flags.

- APOGEE_MIRCLUSTER_STAR
- APOGEE_EMISSION_STAR
- APOGEE_EMBEDDEDCLUSTER_STAR
- young cluster (IN-SYNC)
- APOGEE2_W345
- EB planet

This cut isolates a clean sample of $\sim 12,000$ subgiants. I furthermore isolate the low and high- α sequences with the cut

$$\begin{cases} [\text{Mg}/\text{Fe}] > 0.12 - 0.13 [\text{Fe}/\text{H}], & [\text{Fe}/\text{H}] < 0 \\ [\text{Mg}/\text{Fe}] > 0.12, & [\text{Fe}/\text{H}] > 0. \end{cases} \quad (21)$$

The low- α sequence is better reproduced by this model, so I use this cut of the subgiants to compare the models against except for comparing $[\text{C}/\text{Mg}]$ - $[\text{Mg}/\text{Fe}]$.

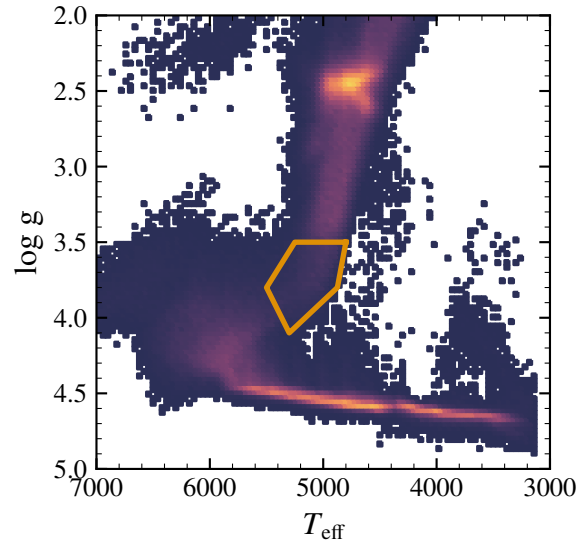
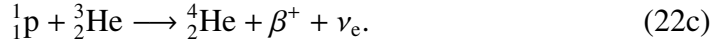


Figure 15: A Kiel diagram of APOGEE stars. Following Roberts et al. (2023, in prep.), I select subgiants in the orange polygon (see Equation 20). These stars have not yet experienced first dredge-up, so their photospheric C and N abundances should reflect their birth mixture.

B. Low-Mass Stellar Evolution

For reference, I include here a brief summary of the physics behind carbon production in low-mass stars. Low-mass stars ($\lesssim 8M_{\odot}$, like our sun), are born when they are fusing H into He. Typically, the dominant process is through the aptly named *pp chain*, which takes four protons ${}^1_1\text{p}$ and releases a He nucleus α , positrons β^+ , photons γ , and electron neutrinos ν_e .



However, when the core temperature becomes high enough, the CNO cycle begins to activate. Starting with ${}^{12}\text{C}$, the CNO cycle is a series of proton captures that result in the creation of a new He nucleus.



(There are other less important minor branches of the CNO cycle cycle (Adelberger et al. 2011).) The CNO cycle is more intense at high metallicities, as the abundance of ${}^{12}\text{C}$ is higher. Since the slowest reaction in the CNO cycle is the ${}^{14}\text{N}$ proton capture (Eq. 23d; also see Adelberger et al. 2011), the net effect is to convert ${}^{12}\text{C}$ into ${}^{14}\text{N}$.

After the end of the main sequence (core H burning), a star begins to ascend the red giant branch. The star first becomes a subgiant, slightly more luminous and redder than the main sequence. Then, first dredge up occurs when the contracting

core drives convection currents through, bringing processed material from the core to the surface. Because of the CNO cycle, the surface abundances of C will be lowered and N enhanced.

Stars with masses $\gtrsim 0.6M_{\odot}$ build up a large He core during the red giant branch. Eventually, conditions are dense and hot enough for He to begin to fuse, and the star now enters the He-burning phase. (Second dredge-up occurs during this transition.) As the next (accessible) stable isotope after He is C, the primary process to fuse He is through the triple- α process, where three He nuclei are combined to form ^{12}C .



Additionally, some $^{12}_6\text{C}$ may furthermore fuse into O through $\alpha + {}^{12}_6\text{C} \longrightarrow {}^{16}_8\text{O} + \gamma$.

When the star's core becomes full of C and O, the star finally enters the asymptotic giant branch phase (AGB). (Only the most massive low-mass stars burn further than O, creating some Mg, but these stars are a small fraction of low-mass stars.) An AGB star has a more complex structure, with an inert core, a He-burning shell, and an outer H-burning shell. The double shell structure causes instabilities towards the end of the AGB phase. In this thermally pulsating phase, each pulse begins with a He-flash (where the He-shell becomes much more luminous). This flash causes the star to expand, driving convective currents that dredge up material from the CO core (third dredge up), and fusion stops temporarily. The star settles again and stays stable for several Myrs until the cycle repeats. During each He-flash, some material from the stellar surface is lost. This mass-loss is the source of AGB enrichment. Finally, the star loses enough mass such that the thermal pulses stop. The star becomes a white dwarf, left to cool for eternity.

C. Oxygen and Magnesium

As I focus on constraining relative yields, I neglect O and Mg yield variations in the main text (excluding the uniform scaling of yields and mass loading in Section 5.5). There is substantial variation in predicted Mg yields (see Fig. 16). Most models predict relatively flat trends metallicity (even with rotation as in Limongi & Chieffi 2018). However, the variation is significant and my adopted $y_{\text{Mg}}^{\text{CC}}$ yield is much higher than most models. This is a known problem (see Griffith et al. 2021). CCSNE models underpredict $[\text{Mg}/\text{O}]$, and the reason why is unknown. My results are independent of the choice of CCSNE element as I assume $[\text{Mg}/\text{O}] = 0$.

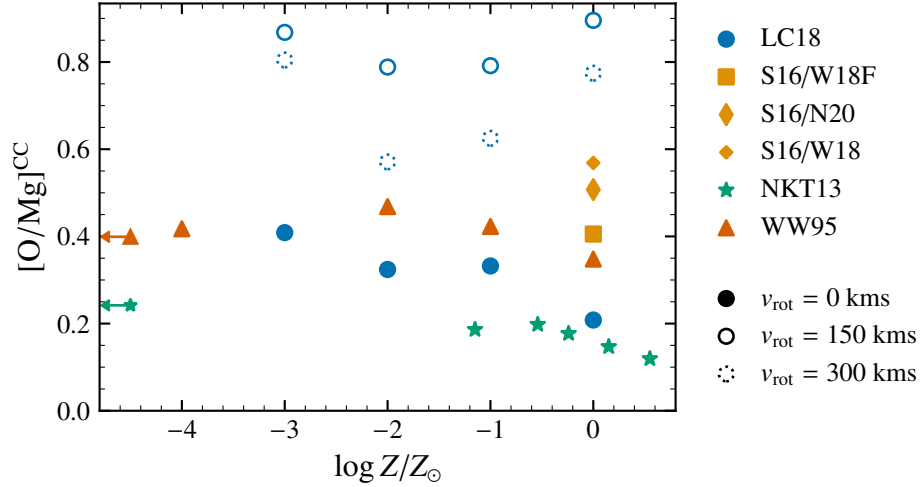


Figure 16: Similar to the top panel of Fig. 5, but for Mg.

D. Software

Software that has contributed to this work:

- Ohio Supercomputer Center (1987)
- VICE (Johnson & Weinberg 2020; Johnson et al. 2021)
- `matplotlib` (Hunter 2007)
- `scipy` (Virtanen et al. 2020)
- IPython (Pérez & Granger 2007)
- `pandas` (pandas development team 2020)
- `numpy` (Harris et al. 2020)
- `astropy` (Astropy Collaboration et al. 2013, 2018, 2022)
- `seaborn` (Waskom 2021)

E. Low-Mass Stellar Yield Models

C11 is from Cristallo et al. (2011, 2015), V13 from Ventura et al. (2013, 2014, 2018); Vincenzo et al. (2021), K10 from Karakas (2010), and K16 from Karakas & Lugaro (2016); Karakas et al. (2018)

model	Masses/ M_{\odot}	Z
C11	1.3, 1.5, 2.0, 2.5, 3.0, 4.0, 5.0, 6.0	0.0001, 0.0003, 0.001, 0.002, 0.003, 0.006, 0.008, 0.01, 0.014, 0.02
K10	1.0, 1.25, 1.5, 1.75, 1.9, 2.25, 2.5, 3.0, 3.5, 4.0, 4.5, 5.0, 5.5, 6.0	0.0001, 0.004, 0.008, 0.02.
V13	1.5, 2.0, 2.5, 3.0, 3.5, 4.0, 4.5, 5.0, 6.0, 6.5, 7.0	0.0003, 0.001, 0.002, 0.004, 0.008, 0.014, 0.04
K16	1.0, 1.25, 1.5, 1.75, 2.25, 2.5, 2.75, 3.0, 3.25, 3.5, 3.75, 4.0, 4.5, 5.0, 5.5, 6.0, 7.0	0.0003, 0.001, 0.002, 0.004, 0.008, 0.014, 0.04

F. Symbols

$[A/B]$	The abundance ratio between elements A and B . $[A/B] = \log_{10}(A/B) - \log_{10}(A_{\odot}/B_{\odot})$, i.e. $[A/B]$ is the logarithm of the ratio between A and B , scales such that $[A/B] = 0$ for the sun. Solar abundances are as measured in Asplund et al. (2009).
α_{AGB}	The multiplicative increase in AGB C production. See Eq. 12.
α_{CC}	The multiplicative increase in CCSNE C production. See Eq. 12.
η	The mass outflow loading factor. η is the ratio between ejected gas from the galaxy and star formation, i.e. $\eta = \dot{M}_{\text{outflow}}/\dot{M}_{\star}$.
ζ	The high-mass star carbon yield metallicity dependence. See Eq. 13.
$\dot{\Sigma}$	The surface mass density of star formation.
M	The mass of a star, in units of M_{\odot}
M_{\odot}	The mass of the sun. $M_{\odot} = 1.989 \times 10^{33}$ g.
\dot{M}_{\star}	The rate of star formation (mass of new stars per time interval).
\dot{M}_X	The rate of change of the mass of element X .
f_{AGB}	The fractional contribution of AGB stars to the total IMF-averaged carbon yield at solar metallicity. See Eq. 17
R	The galactocentric radius (distance from the galactic center) in kpc.

\tilde{y}_C^{AGB}	The per-star yield of C from low-mass stars of a given mass. In other words, the amount of new C an AGB star ejects divided by the initial mass of the star.
y_C^{AGB}	The IMF-averaged yield of C from low-mass stars.
y_C^{CC}	The IMF-averaged yield of C from high-mass stars.
$y_{\text{Mg}}^{\text{CC}}$	The IMF-averaged yield of Mg.
Z_{\odot}	The metallicity for the sun. $Z_{\odot} = 0.014$.
Z	The metallicity fraction, i.e. the mass fraction of all elements which are not H or He.
Z_X	The mass fraction of element X.

Acronyms

- AGB** Asymptotic giant branch stars. The AGB phase is the last phase of low-mass stars, before stars become white dwarfs. Produces C, N, and heavy s-process elements. See Appendix B..
- APOGEE** Apache Point Observatory Galactic Evolution Experiment. A large near-infrared spectroscopic survey of stars in the Milky Way. (Majewski et al. 2017).
- CCSNE** Core collapse supernovae. Massive star explosions. CCSNE produce many elements including α -element, Fe-peak elements, and r and s-process elements.
- DLA** Damped Lyman-alpha system. DLAs are clouds of gas from the early universe which are observed through their absorption of quasar spectra. The name comes from the strong Lyman-alpha lines (1216Å) due to H absorption.
- GCE** Galactic chemical evolution.
- IMF** Initial mass function. A function describing the mass distribution of newly formed stars. I use a Kroupa (2001) IMF, which is described as a piecewise power-law function of M .
- SFH** Star formation history.
- SNE IA** Type Ia Supernovae. Exploding white dwarfs. Produces Fe-peak elements and has a long delay time.
- SSP** Single stellar population. A group of stars formed all at the same time.

Glossary

α -element Elements which are made up of α -particles (He nuclei) through the triple- α process (see Eq. 24). Essentially light, even-numbered elements like O, Mg, and Na. §1.0, 5.7, F.0

IMF-averaged Averaged over the initial-mass function (IMF). The IMF-weighted yield is the mass of the newly produced element divided by the mass of star formation for a single stellar population (see SSP). §2.0, 2.1, 3.0, 5.3, F.0

insideout Our fiducial star formation history. The rate of star formation is highest towards the center of the galaxy and at earlier times. See Eq. 14. §4.0, 5.4

CNO cycle A proton-fusion cycle which occurs in red giant branch stars consisting of a chain of proton captures releasing a He nucleus (α -particle) and energy. See Eq. 23. §B.0

delay time distribution The distribution in time of when an element is produced after a star formation event. §2.0, 2.1, 5.2, 5.3

Fe-peak elements Fe and nearby elements, produced in CCSNE and SNE IA. §F.0

first dredge up First dredge up occurs when a low-mass star enters the red giant branch phase. Material from the core is brought to the surface, increasing N and decreasing C abundances. See Appendix B. §1.0, 5.1, A.0, B.0

high- α The high- α sequence, as described by Eq. 21. §5.7, A.0

high-mass star Stars with masses $\lesssim 8 M_{\odot}$, which end as a neutron star, black hole, or supernovae. §2.1, 2.2, 5.5, 6.0, F.0

hot bottom burning Hot bottom burning occurs inside AGB stars. The base of the convective envelope becomes hot enough for CNO burning to initiate. §2.1

low- α The low- α sequence, as described by Eq. 21. §1.0, 5.1, 5.6, A.0

- low-mass star** Stars with masses $\lesssim 8 M_{\odot}$ which end life as a white dwarf. §2.0, 2.1, B.0, F.0
- mass loading** The strength of outflows relative to star formation. See also η . §C.0
- metallicity** the (mass) fraction of a star or gas which is not made of either H or He. For the sun, the metallicity is $Z_{\odot} = 0.014$ §1.0, 2.1
- multi-zone** A chemical evolution model where a galaxy is divided into several zones, each with different stars, gas, and properties. §4.0, 6.0
- nucleosynthesis** The synthesis of new elements through fusion inside stars. See Appendix B. §2.0, 6.0
- one-zone** A chemical evolution model where the gas is all the same composition, i.e. neglecting spatial variations. §3.0, 4.0
- red giant branch** Red giant branch stars are stars that have completed hydrogen core burning and have expanded in size. See Appendix B. §1.0, 5.1, A.0, B.0, F.0
- s-process elements** Elements produced through slow neutron captures, typically in AGB stars. §F.0
- subgiant** A star in the process of leaving the main sequence and becoming a red giant branch. §1.0, 3.1, 5.1, 5.6, 6.0, A.0, B.0
- third dredge up** Third dredge up occurs inside AGB stars. During each thermal pulse, material is *dredged up* from the core, changing the chemical abundances of the stellar atmosphere. (While nominally called *third dredge up*, there are typically several third dredge ups.). See Appendix B. §2.1, B.0
- yield** The net production of a new element during a star’s lifecycle divided by the star’s mass (including winds and supernovae ejecta). §1.0, 2.0